

# A model-independent analysis of leptophilic dark matter at future electron-positron colliders in the mono-photon and mono- $Z$ channels

Saumyen Kundu,<sup>a,1</sup> Atanu Guha,<sup>b,c</sup> Prasanta Kumar Das,<sup>a</sup> P. S. Bhupal Dev<sup>d</sup>

<sup>a</sup>*Department of Physics, Birla Institute of Technology and Science Pilani, K K Birla Goa Campus, NH-17B, Zuarinagar, Goa 403726, India*

<sup>b</sup>*Indian Institute of Science Education and Research Pune, Dr. Homi Bhabha Road, Ward No. 8, NCL Colony, Pashan, Pune 411008, India*

<sup>c</sup>*Department of Physics and Institute of Quantum Systems (IQS), Chungnam National University, Daejeon 34134, Republic of Korea*

<sup>d</sup>*Department of Physics and McDonnell Center for the Space Sciences, Washington University, St. Louis, MO 63130, USA*

*E-mail:* [p20170022@goa.bits-pilani.ac.in](mailto:p20170022@goa.bits-pilani.ac.in), [atanu.guha@iiserpune.ac.in](mailto:atanu.guha@iiserpune.ac.in),  
[pdas@goa.bits-pilani.ac.in](mailto:pdas@goa.bits-pilani.ac.in), [bdev@wustl.edu](mailto:bdev@wustl.edu)

**ABSTRACT:** We consider the possibility that dark matter (DM) only interacts with the Standard Model leptons, but not quarks at tree-level, and analyze the future lepton collider prospects of such leptophilic DM in the mono-photon and mono- $Z$  (both leptonic and hadronic) channels. Adopting a model-independent effective field theory framework, we consider all possible dimension-6 operators of scalar-pseudoscalar (S-P), vector-axialvector (V-A) and tensor-axialtensor (T-AT) types for a fermionic DM and derive the collider sensitivities on the effective cut-off scale  $\Lambda$  as a function of the DM mass. As a concrete example, we take the beam configurations of the International Linear Collider with  $\sqrt{s} = 1$  TeV and  $1000 \text{ fb}^{-1}$  integrated luminosity, including the effect of beam polarization, and show that it can probe leptophilic DM at  $3\sigma$  level up to  $\Lambda$  values of 4.8 TeV, 6.5 TeV and 5.3 TeV for the S-P, V-A and T-AT type operators respectively. This is largely complementary to the direct and indirect searches for leptophilic DM, and can potentially provide the best-ever sensitivity in the low-mass DM regime.

**KEYWORDS:** Dark Matter, Effective Field Theory, Lepton Collider

---

<sup>1</sup>Corresponding author.

---

## Contents

<b>1</b>	<b>Introduction</b>	<b>1</b>
<b>2</b>	<b>Effective operators</b>	<b>4</b>
<b>3</b>	<b>Mono-photon channel</b>	<b>6</b>
3.1	Cross-sections	7
3.2	Effect of polarization	7
3.3	Cut-based analysis	9
3.4	Signal significance	15
<b>4</b>	<b>Mono-<math>Z</math> channel</b>	<b>19</b>
4.1	Leptonic mode	19
4.1.1	Unpolarized and polarized cross-sections	19
4.1.2	Cut-based analysis	21
4.1.3	Results	26
4.2	Hadronic mode	27
4.2.1	Unpolarized and polarized cross-sections	28
4.2.2	Cut-based analysis	29
4.2.3	Results	35
<b>5</b>	<b>Conclusion</b>	<b>38</b>
<b>A</b>	<b>Kinematic distributions for polarized beams</b>	<b>38</b>

---

## 1 Introduction

There is overwhelming evidence for the existence of dark matter (DM) in our Universe from various astrophysical and cosmological observations, such as galactic rotation curves, velocities of stars in dwarf galaxies, velocities of galaxies in clusters, hot gas in galaxy clusters, collisions of galaxy clusters, gravitational lensing, cosmic microwave background (CMB) and large scale structure measurements (see e.g. Refs. [1, 2] and references therein). However, apart from its gravitational interaction and the fact that it constitutes 26.8% of the total energy budget of the Universe [3], very little is known about the true nature and properties of DM. On the theory front, there exists a plethora of particle DM candidates [4] and identifying the correct one is a pressing issue in beyond the Standard Model (BSM) physics. On the experimental front, a number of ongoing and planned efforts in direct [5], indirect [6] and collider [7] searches for DM are poised to shed more light on the DM mystery [8].

Most of the current DM searches are traditionally motivated by the so-called ‘WIMP miracle’ (see e.g. Ref. [9]) – the simple observation that an electrically neutral, cosmologically stable Weakly Interacting Massive Particle (WIMP)  $\chi$  with mass around the electroweak scale and couplings of the order of weak coupling strength to the SM sector can successfully reproduce the observed DM relic density of  $\Omega_\chi h^2 = 0.120 \pm 0.001$  [3]. The WIMP DM mass can actually be in a wide range varying from  $\mathcal{O}(1)$  MeV to  $\mathcal{O}(100)$  TeV, although the possibility of an electroweak scale mass is much more appealing as a host of well-motivated BSM scenarios, from the supersymmetric extensions to the extra dimension models, can easily accommodate such a WIMP DM. The robustness of the WIMP paradigm comes from the fact that the interactions of the WIMP with the SM keep it in thermal equilibrium at high temperatures in the early universe. Later as the universe expands and cools, the rate of interaction of WIMP with the SM sector falls below the Hubble expansion rate, and as a result, the WIMP DM decouples (‘freezes out’) from the thermal plasma and explains the observed relic density in the present universe.

However, the WIMP paradigm is under significant strain, as the stringent exclusion limits from DM direct detection experiments, such as LUX [10], XENON1T [11] and PANDAX-4T [12] have pushed the WIMP parameter space down to an awkward corner fast approaching the neutrino floor [13, 14], below which it will be extremely challenging to disentangle the DM signal from the coherent neutrino background. Therefore, it is important to explore other DM ideas that could potentially explain the absence of a signal in these experiments, while having promising prospects at other experiments. It is interesting to note that a majority of the existing experimental constraints crucially rely on the WIMP interactions with nucleons, and therefore, can be largely weakened if the WIMP predominantly interacts with the SM leptons, but not quarks at tree-level. Such *leptophilic* DM could indeed arise naturally in many BSM scenarios [15–59], some of which could even explain various experimental anomalies, such as the muon anomalous magnetic moment [60, 61], DAMA/LIBRA annual modulation [62], anomalous cosmic ray positron excess as observed in ATIC [63], PAMELA [64, 65], Fermi-LAT [66, 67], AMS-02 [68–70], DAMPE [71] and CALET [72], the galactic center gamma-ray excess [73], 511 keV gamma-ray line [74], IceCube ultra-high energy neutrino excess [75], and XENON1T electron excess [76]. Dedicated searches for leptophilic DM in direct detection experiments [77–79], beam dump experiments [80, 81], gravitational wave detectors [53], as well as using terrestrial [82] and celestial objects like sun [83, 84], supernova [85] and neutron stars [86–90] have also been discussed.

In this paper, we focus on the leptophilic DM searches at colliders, which are complementary to the direct and indirect detection searches. In order to keep our discussion as general as possible, we will adopt an effective field theory (EFT) approach, which has been widely used in the context of collider searches for DM following the early works of Refs. [29, 91–98] (see Ref. [99] for a review). The same interactions responsible for WIMP DM pair-annihilation in the early universe leading to their thermal freeze-out guarantee their direct production at colliders, as long as kinematically allowed. This will give a characteristic mono- $X$  signature, where the large missing transverse momentum carried away by the DM pair is balanced by a visible sector particle  $X$  (which can be either a photon,

jet,  $W$ ,  $Z$ , or Higgs, depending on the model) emitted from an initial, intermediate or final state (see Refs. [99, 100] for reviews). Specifically, the mono-jet signature has become emblematic for LHC DM searches [101–104]. However, for a leptophilic DM with loop-suppressed interactions to the SM quarks, the hadron colliders like the LHC are not expected to provide a better model-independent limit than the existing constraints from indirect searches, such as from AMS-02 [105, 106], at least within the EFT framework with contact interactions.

On the other hand, lepton colliders provide an ideal testing ground for the direct production of leptophilic DM and its subsequent detection via either mono-photon [95, 98, 107–116] or mono- $Z$  [117–120] signatures. In this paper, we go beyond the existing literature and perform a comprehensive and comparative study of both mono-photon and mono- $Z$  signatures of leptophilic DM at future  $e^+e^-$  colliders in a model-independent, EFT approach. Our analysis is generically applicable to all future  $e^+e^-$  colliders, such as the ILC [121], CLIC [122], CEPC [123] and FCC-ee [124], but for concreteness, we have taken the  $\sqrt{s} = 1$  TeV ILC as our case study for numerical simulations. We also assume the DM to be fermionic and limit ourselves to the dimension-6 operators, but taking into consideration all possible dimension-6 operators of scalar-pseudoscalar (S-P), vector-axialvector (V-A) and tensor-axialtensor (T-AT) type as applicable for the most general DM-electron coupling. Within the minimal EFT approach, the only relevant degrees of freedom in our analysis are the DM mass and an effective cut-off scale  $\Lambda$  which determines the strength of the four-Fermi operators. This enables us to derive model-independent ILC sensitivities on leptophilic DM in the  $(m_\chi, \Lambda)$  plane in both mono-photon and mono- $Z$  (leptonic and hadronic) channels, after taking into account all relevant backgrounds and systematic uncertainties. We consider both unpolarized and polarized beam options [121, 125], and find that with the proper choice of polarizations for the  $e^-$  and  $e^+$  beams (which depends on the operator type), the DM sensitivities could be significantly enhanced. We also find that the hadronic mono- $Z$  channel provides the best sensitivities for the S-P and T-AT type operators, while the mono-photon channel gives better sensitivity for the V-A type operators. For example, for a 1 GeV DM mass, the mono-photon channel can probe  $\Lambda$  values at  $3\sigma$  confidence up to 4.8 TeV, 6.5 TeV and 5.3 TeV for the S-P, V-A and T-AT type operators respectively at  $\sqrt{s} = 1$  TeV ILC with  $1000 \text{ fb}^{-1}$  integrated luminosity, whereas the mono- $Z$  hadronic (leptonic) channel can probe  $\Lambda$  values up to 4.2 (3.2) TeV, 2.7 (2.5) TeV and 5.2 (4.0) TeV respectively. We compare our results with the existing literature wherever applicable and also with the current constraints from direct and indirect detection, as well as from relic density considerations. We find that the  $\sqrt{s} = 1$  TeV ILC sensitivities could surpass the existing constraints for light DM with masses below about 300 GeV, above which the collider reach is weakened mainly due to the kinematic suppression.

The rest of the paper is organized as follows. In Section 2, we briefly describe the EFT approach and list all possible dimension-6 operators for the DM-electron coupling in our leptophilic DM scenario. In Section 3, we present our cut-based analysis for the mono-photon+ $\cancel{E}_T$  signal and background, both with and without beam polarization. In Section 4, we repeat the cut-based analysis for the mono- $Z$ + $\cancel{E}_T$  channel, with the leptonic case of  $Z \rightarrow \ell^+\ell^-$  (with  $\ell = e, \mu$ ) in Section 4.1 and the hadronic case of  $Z \rightarrow$  jets in

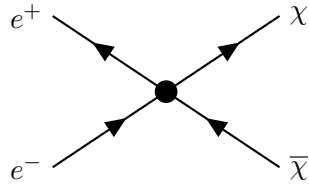


**Figure 1:** Feynman diagram for the effective four-Fermi interactions between the DM and electrons induced by the dimension-6 operator (2.1).

Section 4.2. Our conclusions are given in Section 5.

## 2 Effective operators

Our goal in this paper is to perform a model-independent collider analysis for the leptophilic DM scenario in an EFT approach, with the primary assumptions that (i) the DM particle  $\chi$  couples directly only to the SM leptons but not to the quarks (hence leptophilic), and (ii) the energy scale of the associated new physics is large compared to the collider energies under consideration, thus allowing us to integrate out the heavy mediators and parametrize the DM-SM interactions using effective higher-dimensional operators. For concreteness, we assume that the DM particles are Dirac fermions, and therefore, the leading order DM-SM interactions are the dimension-six four-Fermi interactions shown in Figure 1, with the most-general effective Lagrangian given by [29]

$$\mathcal{L}_{\text{eff}} = \frac{1}{\Lambda^2} \sum_j (\bar{\chi} \Gamma_\chi^j \chi) (\bar{\ell} \Gamma_\ell^j \ell), \quad (2.1)$$

where  $\Lambda$  is the cut-off scale for the EFT description and the index  $j$  corresponds to different Lorentz structures, as shown below. Since our main focus is on  $e^+e^-$  colliders, we will just set  $\ell = e$  in Eq. (2.1) and assume this to be the only leading-order coupling, but our discussion below could be easily extended to other cases, e.g. future muon colliders [126] by setting  $\ell = \mu$ .

A complete set of Lorentz-invariant operators consists of scalar (S), pseudo-scalar (P), vector (V), axial-vector (A), tensor (T) and axial-tensor (AT) currents. We classify them as follows:

$$\begin{aligned} \text{Scalar-Pseudoscalar (S-P) type : } & \quad \Gamma_\chi = c_S^X + ic_P^X \gamma_5, & \quad \Gamma_e = c_S^e + ic_P^e \gamma_5, \\ \text{Vector-Axial vector (V-A) type : } & \quad \Gamma_\chi^\mu = (c_V^X + c_A^X \gamma_5) \gamma^\mu, & \quad \Gamma_{e\mu} = (c_V^e + c_A^e \gamma_5) \gamma_\mu, \\ \text{Tensor-Axial Tensor (T-AT) type : } & \quad \Gamma_\chi^{\mu\nu} = (c_T^X + ic_{AT}^X \gamma_5) \sigma^{\mu\nu}, & \quad \Gamma_{e\mu\nu} = \sigma_{\mu\nu}, \end{aligned} \quad (2.2)$$

where  $\sigma^{\mu\nu} = \frac{i}{2}[\gamma^\mu, \gamma^\nu]$  is the spin tensor and  $c_j^{X,e}$  are dimensionless, real couplings. Note that for the T-AT type, we did not write the AT term for electron separately, because the relation  $\sigma^{\mu\nu} \gamma_5 = \frac{i}{2} \epsilon^{\mu\nu\alpha\beta} \sigma_{\alpha\beta}$  implies that the AT  $\otimes$  AT coupling is equivalent to T  $\otimes$  T, and similarly, T  $\otimes$  AT = AT  $\otimes$  T. Also if we had considered Majorana DM, then vector and T-AT type interactions are forbidden, i.e.  $c_V^X = c_T^X = c_{AT}^X = 0$ . For simplicity, in Eq. (2.1)

we have used a common cut-off scale  $\Lambda$  for all Lorentz structures. Furthermore, in our subsequent numerical analysis, we will consider one type of operator at a time, by setting the corresponding couplings  $c_j^{X,e} = 1$  without loss of generality and all other couplings equal to zero, unless otherwise specified. For instance, setting  $c_S^X = c_P^X = c_S^e = c_P^e = 1$  and all other couplings equal to zero gives us the (S+P)-type operator, which we will simply refer to as the **SP**-type in the following discussion. Similarly, we will denote the  $c_V^X = c_A^X = c_V^e = c_A^e = 1$  case simply as the **VA**-type, and  $c_T^X = c_{AT}^X = 1$  as the **TAT**-type for presenting our numerical results in the  $(m_\chi, \Lambda)$  plane. For other choices of the couplings, our results for the sensitivity on  $\Lambda$  can be easily scaled accordingly.

We do not discuss any specific realization of these effective operators since we are making a model-independent analysis. In the context of a given ultraviolet (UV)-complete theory or even a simplified model, the suppression or cut-off scale  $\Lambda$  of the effective theory can be understood in terms of the mass  $m_{\text{med}}$  of a mediator (which couples to electrons as well as DM) as

$$\frac{1}{\Lambda^2} = \frac{g_e g_\chi}{m_{\text{med}}^2}, \quad (2.3)$$

where  $g_e$  and  $g_\chi$  are the mediator couplings to electron and DM respectively, and the mediator is assumed to be heavier than the energy scale of interest. As a concrete example, let us consider the axial-vector type operator which can be obtained from a theory with a massive spin-1 particle  $V^\mu$  with axial couplings to leptons and DM:

$$\mathcal{L} = \frac{1}{2} m_V^2 V_\mu V^\mu + g_{Ae} \bar{e} \gamma_\mu \gamma^5 e V^\mu + g_{A\chi} \bar{\chi} \gamma_\mu \gamma^5 \chi V^\mu. \quad (2.4)$$

In the context of DM pair-production at lepton colliders via the  $e^+e^- \rightarrow \chi\bar{\chi}$  process,  $V^\mu$  acts as the mediator of the interaction between the electrons and DM particles. For instance, if this is an  $s$ -channel process, then the corresponding matrix element will be

$$\begin{aligned} \mathcal{M} &\sim \left( \frac{g_{Ae} g_{A\chi}}{m_V^2 - s} \right) (\bar{e} \gamma^\mu \gamma^5 e) (\bar{\chi} \gamma_\mu \gamma^5 \chi) \\ &\simeq \left( \frac{g_{Ae} g_{A\chi}}{m_V^2} \right) \left[ 1 + \frac{s}{m_V^2} + \mathcal{O}\left(\frac{s^2}{m_V^4}\right) \right] (\bar{e} \gamma^\mu \gamma^5 e) (\bar{\chi} \gamma_\mu \gamma^5 \chi). \end{aligned} \quad (2.5)$$

In the limit where the center-of-energy is much smaller than the mediator mass, i.e.  $s \ll m_V^2$ , the propagator in Eq. (2.5) will be of the form  $g_{Ae} g_{A\chi} / m_V^2$  which can be simply identified as  $1/\Lambda^2$  in the contact interaction description of EFT [cf. Eq. (2.3)]. On the other hand, if  $m_V^2 \lesssim s$ , the contact interaction Lagrangian (2.1) does not provide an accurate description of the kinematics, because the higher-order terms in Eq. (2.5) can no longer be neglected. Therefore, we will impose a theoretical limit of  $\Lambda > \sqrt{s}$  for the EFT validity. For relatively larger DM mass, we must also have  $\Lambda > 2m_\chi$  in order to describe DM pair annihilation by the EFT. In fact, using  $\Lambda = 2m_\chi$  induces 100% error in the EFT prediction for  $s$ -channel UV completions. Therefore, we will use  $\Lambda > \max\{\sqrt{s}, 3m_\chi\}$  as a conservative lower bound [127] to ensure the validity of our EFT approach.

As opposed to the lepton colliders, the validity of the EFT approach for mono- $X$  searches at the hadron colliders is problematic [128]. Instead, simplified models [129, 130]

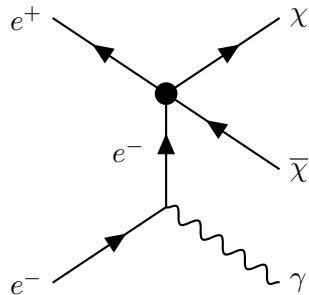


**Figure 2:** Feynman diagram for the mono-photon signal at an  $e^+e^-$  collider. The photon can be radiated off either the electron or the positron leg.

are more appropriate for the interpretation of the LHC results. Therefore, it becomes difficult to directly compare the results from lepton and hadron colliders.

As for the specific model realizations of the other operators listed in Eq. (2.2), the vector-type operator can be easily realized by a similar spin-1 mediator as in Eq. (2.4), with vector instead of axial vector couplings. Similarly, the S-P type operators can be realized by a scalar/pseudoscalar mediator, whereas the T-AT type operators can be realized by a spin-2 mediator. A detailed discussion of these model realizations is beyond the scope of the current work.

### 3 Mono-photon channel

Since DM behaves as missing energy in the collider environment, we need a visible particle along with the DM pair to identify the DM production process. In the context of leptophilic DM at lepton colliders, mono-photon and mono- $Z$  are the most promising channels, where the extra  $\gamma/Z$  comes from initial state radiation (ISR) from either the electron or positron leg. In this section, we analyze the mono-photon signal and backgrounds in detail and present our numerical sensitivity results for  $\sqrt{s} = 1$  TeV ILC with  $1000 \text{ fb}^{-1}$  integrated luminosity. In the next section, we will repeat the same analysis for the mono- $Z$  case.

For the mono-photon signal  $e^+e^- \rightarrow \chi\bar{\chi}\gamma$  (as shown in Figure 2), the  $\chi$ 's will contribute to the missing transverse energy at the detector. The dominant irreducible SM background to this process comes from neutrino pair production with an associated ISR photon, i.e.  $e^+e^- \rightarrow \nu\bar{\nu}\gamma$ . Since neutrinos are practically indistinguishable from WIMPs on an event-by-event basis, the majority of this background survives the event selection cuts. However, as we will show later, this background is highly polarization-dependent, and therefore, can be significantly reduced by the proper choice of polarized beams, without affecting the signal much.

Apart from the neutrino background, any SM process with a single photon in the final state can contribute to the total background if all other visible particles escape detected. The SM processes containing either jets or charged particles are relatively easy to distinguish from a DM event, so their contribution to the total background is negligible [111]. The only exception is the *Bhabha scattering* process associated with an extra photon (either

from initial or final state radiation), i.e.,  $e^+e^- \rightarrow e^+e^-\gamma$ , which has a large cross section, is polarization-independent, and can significantly contribute to the total background whenever the final-state electrons and positrons go undetected, e.g. along beam pipes. In our following analysis, we consider both neutrino and radiative Bhabha backgrounds.

### 3.1 Cross-sections

The cross-sections for the mono-photon signal  $e^+e^- \rightarrow \chi\bar{\chi}\gamma$  and the radiative neutrino background  $e^+e^- \rightarrow \nu\bar{\nu}\gamma$  at  $\sqrt{s} = 1$  TeV ILC are estimated using `CalcHEP` [131] with proper implementation of ISR and beamsstrahlung effects, which significantly affect the width and position of the neutrino  $Z$ -resonance. For this purpose, the EFT Lagrangian (2.1) is implemented in `FeynRules` [132] to generate the CHO library required for `CalcHEP`. To avoid collinear and infrared divergences, we limit the phase space in the event generation with the following cuts on the outgoing photon energy  $E_\gamma$  and its polar angle  $\theta_\gamma$ :

$$8 \text{ GeV} < E_\gamma < 500 \text{ GeV}, \quad |\cos\theta_\gamma| \leq 0.995. \quad (3.1)$$

The *radiative* Bhabha scattering events are generated using `WHIZARD` [133] (to better handle the singularities) with the same set of cuts as in Eq. (3.1) to the matrix element photon (i.e., excluding the ISR and beamsstrahlung photons). Also, some additional cuts are implemented for the Bhabha process to take care of the soft and collinear divergences:

$$M_{e_{\text{in}}^\pm, e_{\text{out}}^\pm} < 2m_e, \quad M_{e_{\text{out}}^\pm, e_{\text{out}}^\pm} < 5 \text{ GeV}, \quad P_T^\gamma > 1 \text{ GeV}, \quad \Delta R_{e^\pm, \gamma} > 0.2, \quad \Delta R_{e^\pm, e^\pm} > 0.4. \quad (3.2)$$

After generating the signal and background events, we perform a fast detector simulation of the `SiD` detector of ILC [134] using `Delphes3` [135] with the configuration card validated in Ref. [136]. The variations of the unpolarized signal cross section as a function of the DM mass and the cut-off scale are shown in Figure 3 left and right panels respectively for all three operator types, namely, SP (solid), VA (dashed) and TAT (dotted)-type. We find that the cross-section is the smallest (largest) for the SP (TAT)-type operator at any given DM mass. In the left panel, the sudden drop in the cross-section as  $m_\chi$  approaches  $\sqrt{s}/2$  is due to phase-space suppression. Otherwise, for smaller DM masses, the cross-section for a given operator type and a given cut-off scale is almost independent of the DM mass. In the right panel, we see that for a given DM mass the cross-section drops as  $\Lambda^{-4}$ , as expected.

As for the background, we find that the neutrino background cross section at  $\sqrt{s} = 1$  TeV is 4.8 pb, while the radiative Bhabha background is 68.4 pb (though it is substantially reduced after the baseline selection). On the other hand, the DM signal cross section is found to be much smaller, as shown in Table 1 for a benchmark DM mass of  $m_\chi = 100$  GeV and the cut-off scale  $\Lambda = 3$  TeV.

### 3.2 Effect of polarization

One important advantage of lepton colliders is that the incoming beams can be polarized. This helps to reduce the neutrino background considerably, as shown in Table 1. To utilize the full advantage of the beam polarization, we investigate the effect of different choices of polarization on the signal and background. At the ILC, the baseline design foresees at



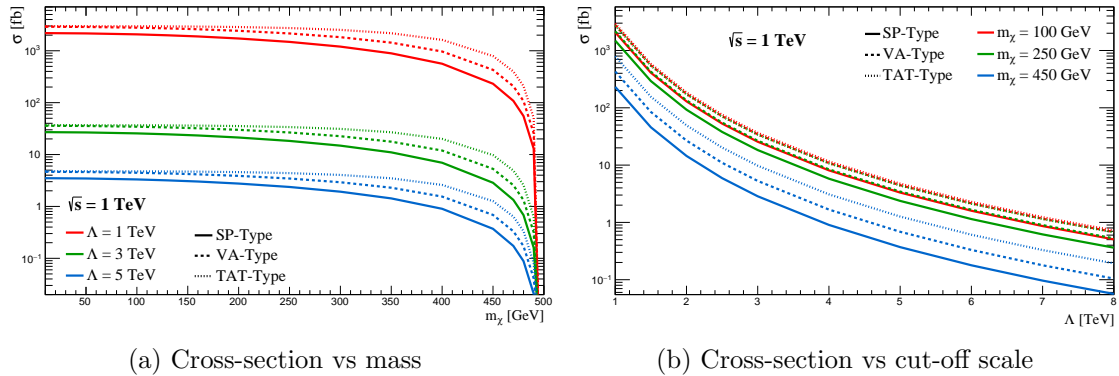


**Figure 3:** Variation of mono-photon signal cross-section with the DM mass (left panel) and the cut-off scale (right panel) at  $\sqrt{s} = 1$  TeV ILC. The solid, dashed and dotted lines are for the SP, VA and TAT-type operators respectively. In the left panel, the red, green and blue curves correspond to different values of the cut-off scale  $\Lambda = 1$  TeV, 3 TeV and 5 TeV respectively, while in the right panel, they correspond to different values of the DM mass  $m_\chi = 100$  GeV, 250 GeV and 450 GeV respectively.

Process type	Unpolarized cross-section (fb)	Polarization $P(e^-, e^+)$	Polarized cross-section (fb)			
			(+, +)	(+, -)	(-, +)	(-, -)
$\nu\bar{\nu}\gamma$	4782	(80, 0)	1106	1106	8506	8506
		(80, 20)	1268	963	10160	6793
		(80, 30)	1393	860	10993	5931
$e^-e^+\gamma$	68439	(80, 0)	67920	67920	68867	68867
		(80, 20)	67909	68386	69285	68297
		(80, 30)	67809	68566	69502	68181
SP-type	25.5	(80, 0)	25.5	25.5	25.5	25.5
		(80, 20)	29.6	21.4	21.4	29.6
		(80, 30)	<b>31.6</b>	19.4	19.4	31.6
VA-type	34.3	(80, 0)	61.7	61.7	6.9	6.9
		(80, 20)	49.4	74.1	5.5	8.2
		(80, 30)	43.2	<b>80.3</b>	4.8	8.9
TAT-type	36.5	(80, 0)	36.5	36.5	36.5	36.5
		(80, 20)	42.3	30.6	30.6	42.3
		(80, 30)	<b>45.2</b>	27.7	27.7	45.2

**Table 1:** Comparison of the SM backgrounds and signal cross sections for the mono-photon channel for the unpolarized beam, as well as for different choices of beam polarization at  $\sqrt{s} = 1$  TeV. For the signal, we have chosen benchmark values of  $m_\chi = 100$  GeV and  $\Lambda = 3$  TeV. The numbers in bold highlight the optimal polarization choice for a given operator type.

least 80% electron beam polarization at the interaction point, whereas the positron beam can be polarized up to 30% for the undulator positron source (up to 60% may be possible with the addition of a photon collimator) [121]. For comparison, we show our results for

three different nominal absolute values of polarization:  $|P(e^-, e^+)| = (80, 0)$ ,  $(80, 20)$  and  $(80, 30)$ . In each case, we can also have four different polarization configurations, namely,  $\text{sign}(P(e^-), P(e^+)) = (+, +)$ ,  $(+, -)$ ,  $(-, +)$  and  $(-, -)$ , where  $+$  and  $-$  denote the right- and left-handed helicities respectively. According to the H20 running scenario, the standard sharing between the different beam helicity configurations is 40% for  $(+, -)$  and  $(-, +)$  each, and 10% for  $(+, +)$  and  $(-, -)$  each [125]. With the luminosity upgrade, the target integrated luminosities per beam helicity configuration is  $3200 \text{ fb}^{-1}$  for  $(+, -)$  and  $(-, +)$  each, and  $800 \text{ fb}^{-1}$  for  $(+, +)$  and  $(-, -)$  each, with the proposed total luminosity of  $8000 \text{ fb}^{-1}$  [125]. However, for the sake of comparison, we just assume  $1000 \text{ fb}^{-1}$  integrated luminosity in each of the four beam helicity configurations.

In Table 1, we show the effect of different schemes of polarizations and helicity orientations on the mono-photon signal and background cross-sections. It is evident from the Table that the radiative Bhabha background remains almost unchanged, as mentioned earlier. On the other hand, electron beam polarization is very effective in reducing the neutrino background, as a 80% *right-handed* electron beam can reduce the neutrino background to 23% of the unpolarized case, even without any polarization on the positron beam. The effect is further enhanced by a *left-handed* positron beam. We see that for 20% and 30% left-handed positron beam polarization, the neutrino background is reduced to 20% and 18% of its unpolarized value, respectively.

The signals are also affected to some extent by beam polarization and the optimal helicity configuration depends on the operator type. For SP- and TAT-type operators we see no effect of electron-beam polarization, but a 20% (30%) *right-handed* positron beam can enhance the signal by 16% (24%). The VA-type signal, on the other hand, prefers the  $(+, -)$  helicity configuration – the same choice for which the neutrino background is minimized. With the  $(+80\%, -30\%)$  configuration, the VA-type signal is enhanced by a factor of 2.3, whereas the  $(+80\%, +30\%)$  configuration enhances it by a modest 26%.

Overall, although the  $(+80\%, -30\%)$  configuration minimizes the background the most, looking at the different signal to background ratio, we find that the  $(+80\%, +30\%)$  configuration is the best for the SP- and TAT-type operators. For direct comparison between the results for different operators, we choose to work with the  $(+80\%, +30\%)$  configuration democratically for all the operator types, unless otherwise specified.

### 3.3 Cut-based analysis

Now we analyze various kinematic distributions and perform a cut-based analysis to optimize the signal-to-background ratio. This of course depends on the DM mass, so in Table 2, we list three benchmark points (BPs) with  $m_\chi = 100 \text{ GeV}$ ,  $250 \text{ GeV}$  and  $350 \text{ GeV}$  respectively, and present the corresponding selection cuts optimized for each case. Here we fix  $\Lambda = 3 \text{ TeV}$  for illustration, but in the next subsection, we will vary both  $m_\chi$  and  $\Lambda$  to obtain the  $3\sigma$  sensitivity limits. As for the choice of the DM mass values, since it was seen from Figure 3 that the signal cross-sections are barely sensitive to the DM mass up to around  $100 \text{ GeV}$ , our BP1 essentially captures the light DM scenario. Similarly, our BP3 is chosen moderately close to the kinematic limit of  $\sqrt{s}/2$  (going too close to  $\sqrt{s}/2$  will result

	<b>BP1</b>	<b>BP2</b>	<b>BP3</b>
<b>Definition</b>	$m_\chi = 100 \text{ GeV},$ $\Lambda = 3 \text{ TeV}$	$m_\chi = 250 \text{ GeV},$ $\Lambda = 3 \text{ TeV}$	$m_\chi = 350 \text{ GeV},$ $\Lambda = 3 \text{ TeV}$
Baseline selection	$E_\gamma > 10 \text{ GeV},  \eta_\gamma  < 2.45, P_T^{\text{miss}} > 10 \text{ GeV}$		
<b>SP-type</b>			
Cut-1	$E_\gamma < 450 \text{ GeV}$	$E_\gamma < 340 \text{ GeV}$	$E_\gamma < 250 \text{ GeV}$
Cut-2	$ \eta_\gamma  < 1.6$		
Cut-3	$P_T^{\text{miss}} < 450 \text{ GeV}$	$P_T^{\text{miss}} < 340 \text{ GeV}$	$P_T^{\text{miss}} < 240 \text{ GeV}$
Cut-4	$P_T^{\text{frac}} < 1.3$		
Cut-5	$1.1 < \Delta R_{\gamma, \text{MET}} < 4.5$		
<b>VA-type</b>			
Cut-1	$E_\gamma < 440 \text{ GeV}$	$E_\gamma < 350 \text{ GeV}$	$E_\gamma < 250 \text{ GeV}$
Cut-2	$ \eta_\gamma  < 1.7$		
Cut-3	$P_T^{\text{miss}} < 400 \text{ GeV}$	$P_T^{\text{miss}} < 340 \text{ GeV}$	$P_T^{\text{miss}} < 250 \text{ GeV}$
Cut-4	$P_T^{\text{frac}} < 1.2$		
Cut-5	$1.1 < \Delta R_{\gamma, \text{MET}} < 4.5$		
<b>TAT-type</b>			
Cut-1	$E_\gamma < 460 \text{ GeV}$	$E_\gamma < 360 \text{ GeV}$	$E_\gamma < 230 \text{ GeV}$
Cut-2	$ \eta_\gamma  < 1.7$		
Cut-3	$P_T^{\text{miss}} < 450 \text{ GeV}$	$P_T^{\text{miss}} < 350 \text{ GeV}$	$P_T^{\text{miss}} < 230 \text{ GeV}$
Cut-4	$P_T^{\text{frac}} < 1.2$		
Cut-5	$1.1 < \Delta R_{\gamma, \text{MET}} < 4.4$		

**Table 2:** Mono-photon selection cuts for different BPs across all operator types. Because of the dynamic nature of these cuts, the backgrounds will have to be separately analyzed for each BP.

in cross-section values too low too low to give sizable event counts after all the selection cuts). The BP2 is chosen for an intermediate mass DM in between BP1 and BP2.

**Baseline selection cuts:** We define our mono-photon signals by those events that pass through the baseline selection criteria as defined below, in addition to the cuts given in Eq. (3.1):

$$E_\gamma > 10 \text{ GeV}, |\eta_\gamma| < 2.45 \text{ and } P_T^{\text{miss}} > 10 \text{ GeV}, \quad (3.3)$$

where the hardest photon in an event is considered as the signal photon. For the radiative Bhabha background, we define the selection criteria for electrons as  $P_{T,e} > 10 \text{ GeV}, |\eta_e| < 2.5$ , and have kept only those events which contain no electrons (and positrons) passing these criteria, which means they have escaped detection.

After implementing these baseline selection cuts, the signal and background cross sections are given (in parentheses) in the first rows of Tables 3 and 4 respectively. We find that the signal and the neutrino background are reduced to about 60% of their original values in Table 1. Similarly, the actual Bhabha-induced background relevant for our signal is found to be only about 13% of its original value quoted in Table 1 after the baseline selection cuts, taking into account only the missed electron events. To further enhance our

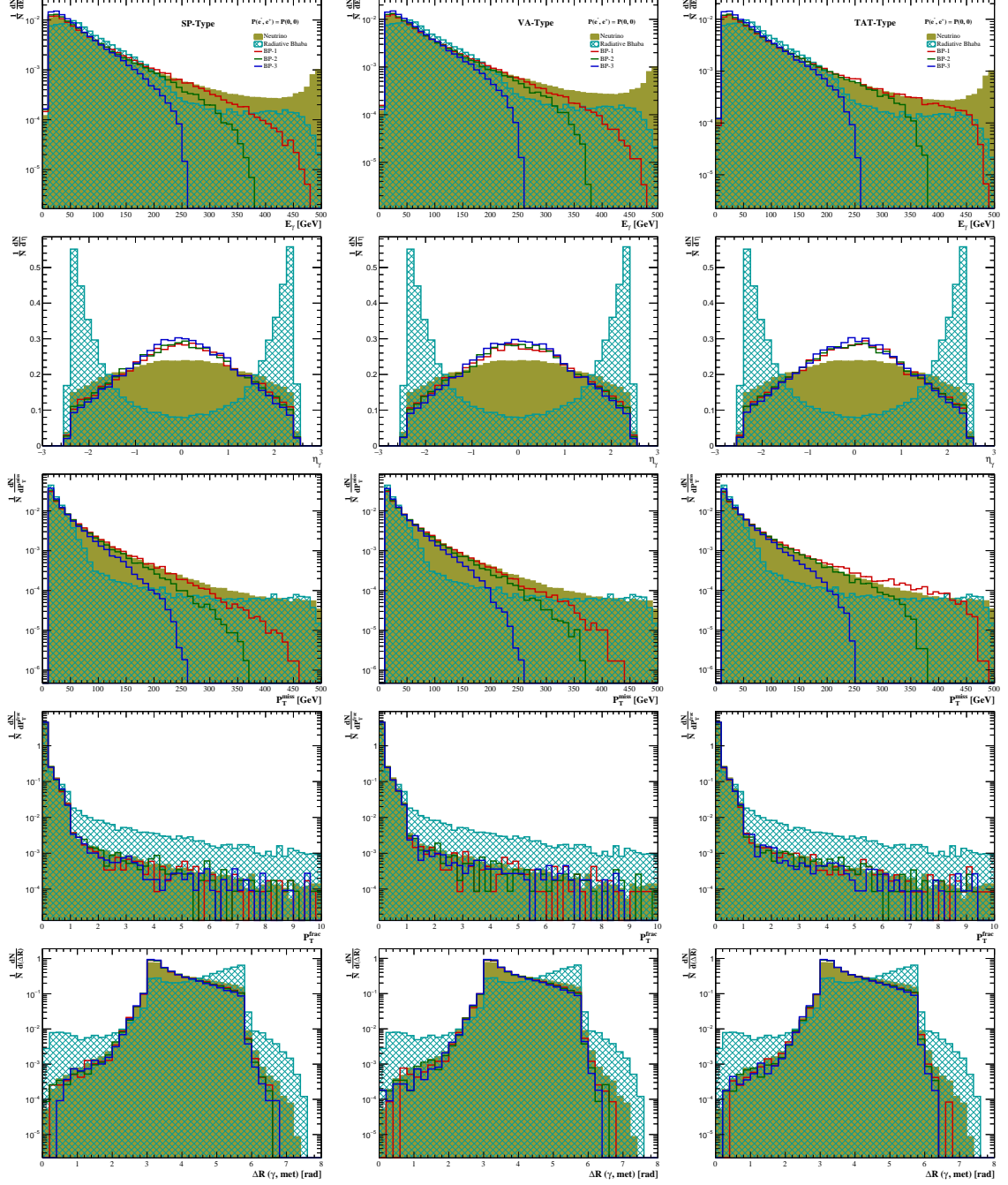


**Figure 4:** Normalized differential distributions after baseline selection cuts for the set of five kinematic observables considered in Table 2, namely,  $E_\gamma$ ,  $\eta^\gamma$ ,  $P_T^{\text{miss}}$ ,  $P_T^{\text{frac}}$  and  $\Delta R_{\gamma, \text{MET}}$  for the unpolarized case (the polarized case histograms are in the Appendix, see Figure 17). In each panel, the shaded green histograms are for the neutrino background and the cyan hatched histograms are for the radiative Bhabha background. The unshaded red, green and blue histograms are for BP1, BP2 and BP3 respectively. The left, middle and right panels correspond to the SP, VA and TAT-type operators respectively.

Selection cuts	Cut efficiencies					
	Unpolarized beams			(+80%, +30%) polarized beams		
	BP-1	BP-2	BP-3	BP-1	BP-2	BP-3
<b>SP-type:</b>						
Baseline selection	100% (14.93 fb)	100% (10.49 fb)	100% (6.02 fb)	100% (18.54 fb)	100% (12.95 fb)	100% (7.45 fb)
Cut-1	99.96%	99.88%	99.98%	99.97%	99.86%	99.99%
Cut-2	77.04%	77.59%	79.12%	76.84%	77.75%	79.41%
Cut-3	77.04%	77.59%	79.12%	76.84%	77.75%	79.41%
Cut-4	76.84%	77.40%	78.93%	76.64%	77.55%	79.25%
Cut-5	76.57%	77.15%	78.70%	76.38%	77.26%	79.00%
<b>VA-type:</b>						
Baseline selection	100% (20.10 fb)	100% (15.40 fb)	100% (12.34 fb)	100% (25.45 fb)	100% (19.35 fb)	100% (18.69 fb)
Cut-1	99.94%	99.92%	99.99%	99.96%	99.91%	99.99%
Cut-2	80.25%	80.94%	82.18%	80.12%	80.99%	82.21%
Cut-3	80.23%	80.94%	82.18%	80.10%	80.99%	82.21%
Cut-4	79.97%	80.67%	82.00%	79.89%	80.73%	82.00%
Cut-5	77.10%	77.85%	79.26%	77.04%	77.87%	79.26%
<b>TAT-type:</b>						
Baseline selection	100% (21.89 fb)	100% (19.80 fb)	100% (15.13 fb)	100% (27.12 fb)	100% (24.47 fb)	100% (18.69 fb)
Cut-1	99.85%	99.94%	99.61%	99.86%	99.93%	99.65%
Cut-2	80.35%	80.52%	81.69%	80.34%	80.81%	81.51%
Cut-3	80.33%	80.51%	81.69%	80.33%	80.79%	81.51%
Cut-4	80.09%	80.26%	81.48%	80.11%	80.54%	81.32%
Cut-5	75.20%	75.21%	76.52%	75.03%	75.25%	76.35%

**Table 3:** Cut-flow chart for different operators and BPs for the mono-photon *signal*. The cut efficiencies are calculated with respect to the baseline selection cuts given in Eq. (3.3), with the corresponding cross-sections shown (in parentheses) in the first row.

signal-to-background ratio, we then examine the signal versus background distributions of some relevant kinematic variables and devise further cuts. The normalized distributions are given in Figure 4 for the unpolarized case. The corresponding distributions for the polarized case are shown in Figure 17 in the Appendix.

From Figure 4, we see some variations of the signal distributions between the three BPs. Therefore, the specialized selection criteria discussed below are dynamic with respect to different BPs, as also summarized in Table 2.

**Cut-1:** From the  $E_\gamma$  distribution in Figure 4 (top row), we see that although the neutrino background is mostly signal-like, it has a large number of events around  $E_\gamma \approx 496$  GeV, due to the radiative return of the  $Z$ -resonance which is determined by  $(s - M_Z^2)/2\sqrt{s}$ . On the other hand, the  $E_\gamma$  distribution for the signal drops at a lower value, depending on the DM mass, due to phase-space suppression. Therefore, we impose a dynamic maximum

Selection cuts	Cut efficiencies											
	Unpolarized beams						(+80%, +30%) polarized beams					
	Neutrino			Radiative Bhabha			Neutrino			Radiative Bhabha		
	BP-1	BP-2	BP-3	BP-1	BP-2	BP-3	BP-1	BP-2	BP-3	BP-1	BP-2	BP-3
BS	100% (2764 fb)			100% (8638 fb)			100% (783 fb)			100% (8595 fb)		
<b>SP-type:</b>												
Cut-1	96.77%	93.69%	89.76%	99.59%	99.07%	96.40%	93.17%	89.13%	85.04%	99.60%	98.06%	96.43%
Cut-2	69.73%	68.29%	66.33%	35.64%	34.67%	33.99%	67.11%	62.06%	62.95%	35.99%	34.98%	34.32%
Cut-3	69.73%	68.28%	66.27%	35.51%	34.59%	33.81%	67.10%	65.04%	62.88%	35.88%	34.90%	34.14%
Cut-4	69.48%	68.03%	66.03%	34.38%	33.51%	32.83%	66.84%	64.79%	62.63%	34.72%	34.79%	33.13%
Cut-5	69.10%	67.68%	65.70%	33.69%	32.85%	32.25%	66.45%	64.44%	62.32%	33.98%	33.08%	32.49%
BeamCal	68.80%	67.38%	65.41%	0.89%	0.87%	0.86%	66.16%	64.16%	62.05%	0.90%	0.88%	0.86%
<b>VA-type:</b>												
Cut-1	96.49%	94.01%	89.76%	99.45%	99.22%	96.40%	92.71%	89.49%	85.04%	99.47%	98.20%	96.43%
Cut-2	73.34%	72.04%	69.71%	39.91%	39.10%	38.32%	70.44%	68.64%	66.14%	40.18%	39.32%	38.56%
Cut-3	73.29%	72.02%	69.68%	39.62%	38.99%	38.14%	70.33%	68.61%	66.10%	39.89%	39.22%	38.39%
Cut-4	73.00%	71.73%	69.40%	38.25%	37.66%	36.90%	70.03%	68.31%	65.81%	38.48%	37.84%	37.10%
Cut-5	69.81%	68.67%	66.53%	34.15%	33.60%	32.96%	66.96%	65.42%	63.13%	34.43%	33.84%	33.20%
BeamCal	69.51%	68.37%	66.24%	0.91%	0.89%	0.87%	66.67%	65.13%	62.86%	0.91%	0.90%	0.88%
<b>TAT-type:</b>												
Cut-1	97.10%	94.31%	88.46%	99.72%	98.34%	95.78%	93.73%	89.83%	83.75%	99.73%	98.34%	95.79%
Cut-2	73.67%	72.20%	68.99%	40.13%	39.16%	38.15%	71.04%	68.83%	65.41%	40.40%	39.40%	38.39%
Cut-3	73.66%	72.19%	68.96%	39.96%	39.06%	37.95%	71.01%	68.80%	65.36%	40.24%	39.30%	38.20%
Cut-4	73.36%	71.90%	68.68%	38.56%	37.73%	36.74%	70.70%	68.50%	65.08%	38.80%	37.91%	36.93%
Cut-5	67.75%	66.51%	63.75%	32.07%	31.28%	30.46%	65.27%	63.37%	60.43%	32.31%	31.47%	30.66%
BeamCal	67.46%	66.22%	63.47%	0.85%	0.83%	0.81%	64.98%	63.10%	60.17%	0.86%	0.83%	0.81%

**Table 4:** Cut-flow chart for different operators and BPs for the mono-photon *backgrounds*. The cut efficiencies are calculated with respect to the baseline selection (BS) cuts given in Eq. (3.3), with the corresponding cross-sections shown (in parentheses) in the first row. Note that depending on the operator type we are interested in for the signal, the selection cuts are different (cf. Table 2). Therefore, the corresponding backgrounds will also vary as shown here.

$E_\gamma$  cut (cf. Table 2). The corresponding cut efficiencies for the signal and backgrounds are given in Tables 3 and 4 respectively.

**Cut-2:** Detection of collinear photons is not possible. The limitation of the detector reflects in the baseline pseudorapidity cut  $|\eta_\gamma| < 2.45$ . But for the purpose of background suppression we choose a stricter  $\eta_\gamma$  cut, based on the  $\eta_\gamma$  distribution in Figure 4 (second row), for different operators as shown in Table 2. This cut is very effective in reducing the Bhabha background significantly (cf. Table 4), although the signal also drops by about 20% (cf. Table 3).

**Cut-3:** Since the neutrinos and electrons have negligible mass compared to the massive DM fermions, the missing transverse momentum  $P_T^{\text{miss}}$  in the backgrounds occupy the whole parameter space available to it kinematically, whereas for the signal it has limited available range due to phase-space suppression. Therefore, the  $P_T^{\text{miss}}$  distribution for the signal varies with the DM mass, as can be seen from Figure 4 (third row), and a dynamic selection cut on  $P_T^{\text{miss}}$  can be imposed according to the operator type, as shown in Table 2.

**Cut-4:** Next we consider fractional  $P_T$  of the emitted photon which is defined as  $P_T^{\text{frac}} = |P_T^{\text{miss}} - P_T^\gamma|/P_T^\gamma$ . Although this variable does not have dramatic cut efficiencies for the backgrounds, it does help to suppress the Bhabha background to some extent. Since detecting a soft photon is highly difficult in practice and most of the direct measurements are possible only for the transverse direction where the detectors are placed concentrically, we use the  $P_T^{\text{frac}}$  as a measure of the softness of the emitted photon, as can be seen from its distributions in Figure 4 (fourth row).

**Cut-5:** Finally we consider the variable  $\Delta R(\gamma, \text{MET}) = \sqrt{(\Delta\eta)^2 + (\Delta\phi)^2}$  between the signal photon and the missing transverse energy (MET). From the distributions in Figure 4 (bottom row), this seems like a good cut to reduce mainly the Bhabha background, although the neutrino background is not affected much. From the histograms in Figure 4, it is evident that the neutrino-pair background is almost identical to the signal, especially in the low DM mass scenario. Therefore, even after implementing the baseline and analysis cuts 1 through 5, the neutrino background can only be reduced to about 40% of its original value in Table 1. Similarly, the radiative Bhabha background, although substantially reduced to about 4% of its original value in Table 1 after the baseline selection and analysis cuts, still remains sizable and comparable to the neutrino background. However, an electromagnetic calorimeter in the very forward direction of the beamline (BeamCal) [137] can further suppress the Bhabha background to the per mille level. To properly incorporate the effect of BeamCal, we have used the selection efficiencies obtained from a full detector simulation performed in Ref. [114] by modeling the complete instrumented region in a realistic way. According to this analysis, the selection efficiency of the Bhabha background after the BeamCal veto only is 2.7%, while that of the neutrino background is between 98% and 99.6%. This is included in the last row of Table 4 for each case. As for the DM signal, we expect it to be basically unaffected (just like the neutrino background) by the BeamCal veto, as it does not contain highly energetic charged particles in the longitudinal direction. Therefore, we do not show this in the cut-flow Table 3.

For the polarized case, after the baseline selection cuts, the Bhabha background remains almost same as in the unpolarized case, as shown in Table 4. The neutrino background, on the other hand, is significantly reduced in the polarized case to about 28% of its unpolarized value (cf. Table 4). The other cut efficiencies are also slightly better for the neutrino background in the polarized case.

As for the signals, from Table 1, we see that the TAT-type operator has the largest cross section to start with, both for the unpolarized as well as for the (+80%, +30%) polarized cases. Even after the baseline selection and the specialized cuts discussed above, the TAT-type signal retains the largest efficiency among the three types, as shown in Table 3. This will be reflected in our signal significance results, as discussed below.

Operator type	Signal significance for $\mathcal{L}_{\text{int}} = 1000 \text{ fb}^{-1}$					
	Unpolarized beams			Polarized beams		
	BP-1	BP-2	BP-3	BP-1	BP-2	BP-3
SP-type	8.1 (0.6)	5.8 (0.4)	3.5 (0.3)	18.1 (2.4)	13.0 (1.7)	7.8 (1.0)
VA-type	10.9 (0.8)	8.5 (0.6)	5.6 (0.4)	24.9 (3.2)	19.4 (2.5)	12.9 (1.7)
TAT-type	11.8 (0.8)	10.8 (0.8)	8.5 (0.6)	26.2 (3.5)	24.1 (3.2)	19.2 (2.6)

**Table 5:** Signal significance in the mono-photon channel at  $\sqrt{s} = 1 \text{ TeV}$  with  $\mathcal{L}_{\text{int}} = 1000 \text{ fb}^{-1}$  integrated luminosity. These are the optimized numbers after implementing all the selection cuts. The values in the parenthesis denote the significances with a 1% background systematic uncertainty.

### 3.4 Signal significance

After implementing all the cuts mentioned above, we calculate the final signal significance for our benchmark scenarios using the definition

$$\text{Sig} = \frac{S}{\sqrt{S + B + (\epsilon B)^2}}, \quad (3.4)$$

where  $S$  and  $B$  are the number of signal and total background events respectively for a given integrated luminosity, and  $\epsilon$  is the background systematic uncertainty. Our results are given in Table 5 for the three BPs. We show the numbers for an ideal case with zero systematics and also for a more realistic case with 1% systematics, i.e. with  $\epsilon = 0.01$  (in parentheses). The results are significantly weakened in the latter case because of the relatively large background compared to the signal.

From Table 5, we see that the significance enhances as we go to lower DM mass regions, as expected because of kinematic reasons. Operator-wise we see that TAT and VA-type operators perform better than the SP-type. We also find substantial (around 50%) increase in significance on application of optimal beam polarization. Using a multivariate analysis might improve the signal significance over that obtained here using a simple cut-based analysis, but a detailed TMVA analysis [138] is beyond the scope of the current work and will be reported in a follow-up study.

Going beyond the three BPs, we now vary the DM mass and calculate the signal significance following the same cut-based analysis procedure outlined above. Our results for the  $3\sigma$  sensitivity contours in the  $(m_\chi, \Lambda)$  plane are shown in Figure 5 for all the operator types. The solid (dashed) contours are for the unpolarized (optimally polarized) case, and the blue (green) contours are assuming zero (1%) background systematics. The shaded regions are excluded by various constraints, as follows: First of all, for  $\Lambda < \max\{\sqrt{s}/2, 3m_\chi\}$ , our EFT framework is not valid (cf. Section 2). This is shown by the navy blue-shaded regions in Figure 5. For  $\sqrt{s} = 1 \text{ TeV}$  as considered here, this EFT validity limit supersedes the previous LEP limit [95].

The same effective operator given in Eq. (2.1) also gives rise to DM scattering with electrons  $\chi e^- \rightarrow \chi e^-$ . The exact analytic expressions for these cross sections in our EFT



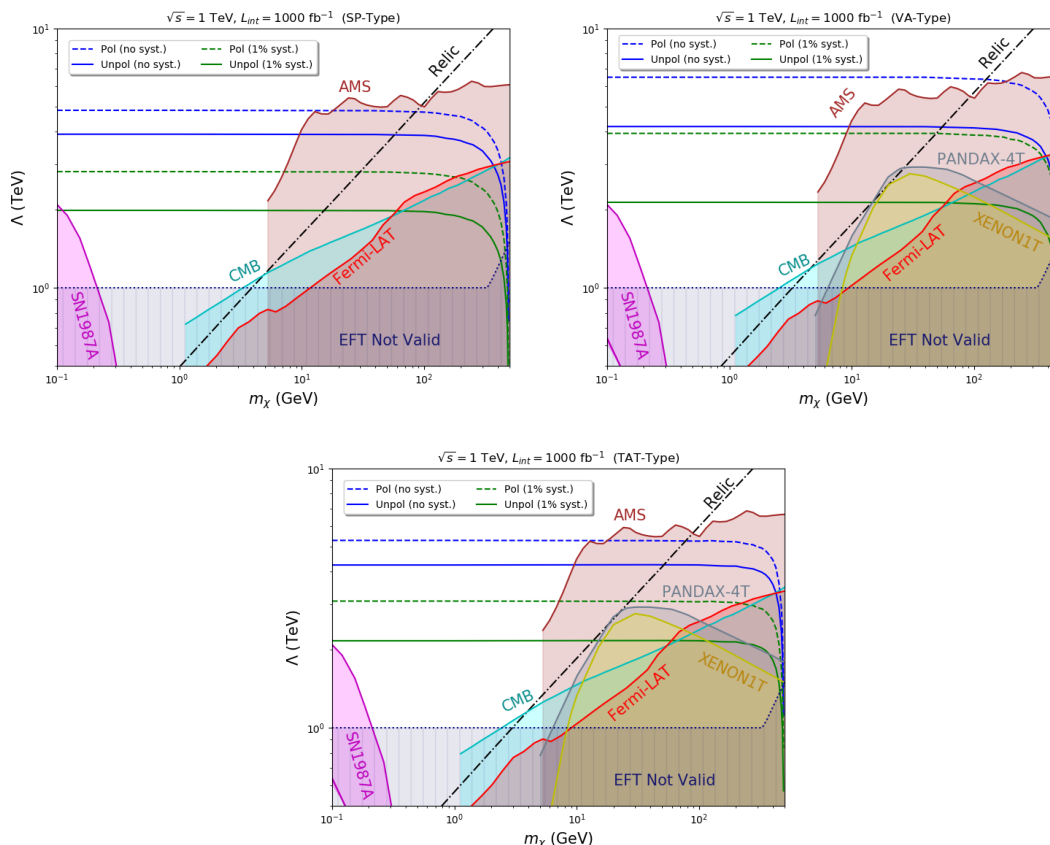


**Figure 5:**  $3\sigma$  sensitivity contours in the mono-photon channel for the SP (top left panel), VA (top right panel) and TAT (bottom panel)-type operators with *unpolarized* (solid lines) and *polarized* (dashed lines)  $e^+e^-$  beams at  $\sqrt{s} = 1$  TeV center-of-mass energy and with  $\mathcal{L}_{\text{int}} = 1000 \text{ fb}^{-1}$  integrated luminosity. The blue (green) contours are assuming zero (1%) background systematics. The various shaded regions are excluded by direct detection (XENON1T, PANDAX-4T), indirect detection (Fermi-LAT, AMS), astrophysics (SN1987A) and cosmology (CMB) constraints. In the shaded region below  $\Lambda = \max\{\sqrt{s}/2, 3m_\chi\}$ , our EFT framework is not valid. Along the dot-dashed line, the observed DM relic density is reproduced for a thermal WIMP assuming only DM-electron effective coupling.

framework can be found in Appendix C of Ref. [85] for all the operator types. Up to velocity or electron mass suppression, the typical size of the cross section is given by

$$\sigma_{\chi e}^0 \simeq \frac{m_e^2}{\pi \Lambda^4} \approx 3.2 \times 10^{-47} \text{ cm}^2 \left( \frac{1 \text{ TeV}}{\Lambda} \right)^4. \quad (3.5)$$

Comparing this with the experimental upper limits on  $\sigma_{\chi e}$  from dedicated direct detection experiments [77, 78], we can derive a *lower* limit on the cut-off scale  $\Lambda$  as a function of the DM mass  $m_\chi$ . However, the current best limit on  $\sigma_{\chi e}$  from XENON1T is at the level of  $\mathcal{O}(10^{-39}) \text{ cm}^2$  [78], which translates into a very weak bound on  $\Lambda$  and is not relevant

for our study. Even the future ambitious proposals like DARKSPHERE can only reach up to  $\mathcal{O}(10^{-42}) \text{ cm}^2$  [139], still 5 orders of magnitude weaker than that needed to probe a TeV-scale  $\Lambda$  value (cf. Eq. (3.5)).

However, more stringent limits can be derived from DM-nucleon scattering searches. Even for a leptophilic DM as in our case, DM-nucleon couplings are necessarily induced at loop level from photon exchange between virtual leptons and the quarks. In fact, as shown in Ref. [29], the loop-induced DM-nucleon scattering almost always dominates over the DM-electron scattering. The analytic expressions for the one and two-loop DM-nucleon scattering cross sections can be found in Ref. [29]. The typical size of the one-loop cross section is [116]

$$\sigma_{\chi N}^1 \simeq \frac{\mu_N^2 c_e^2}{9\pi A^2} \left( \frac{\alpha_{\text{em}} Z}{\pi \Lambda^2} \right)^2 \left[ \log \left( \frac{\Lambda^2}{\Lambda_{\text{NR}}^2} \right) \right]^2 \approx 1.5 \times 10^{-45} \text{ cm}^2 \left( \frac{\mu_N}{10 \text{ GeV}} \right)^2 \left( \frac{1 \text{ TeV}}{\Lambda} \right)^4, \quad (3.6)$$

where  $\mu_N = m_N m_\chi / (m_N + m_\chi)$  is the reduced mass of the DM-nucleon system,  $Z$  and  $A$  are respectively the atomic number and atomic mass of the given nucleus,  $\alpha_{\text{em}}$  is the fine-structure constant,  $\Lambda_{\text{NR}}$  is the direct detection scale, and  $c_e$  is the operator coefficient value at the scale  $\Lambda_{\text{NR}}$ . In the last step of Eq. (3.6), we have used  $\Lambda_{\text{NR}} = 2 \text{ GeV}$  and  $c_e = 0.965$  following Ref. [116]. Since the most stringent DM-nucleon spin-independent cross section limits come from XENON1T [11] and PANDAX-4T [12] experiments, we have also set  $Z = 54$  and  $A = 131$  for the Xenon nucleus, and have translated the experimental upper limits onto the  $(m_\chi, \Lambda)$  plane, as shown by the yellow and grey-shaded regions respectively in Figure 5. Note that these limits are only applicable for the vector and tensor lepton currents, i.e.  $\Gamma_\ell = \gamma_\mu, \sigma_{\mu\nu}$  in Eq. (2.1). For the scalar lepton current,  $\Gamma_\ell = 1$ , the one-loop DM-nucleon coupling vanishes, and one has to go to two loops which is suppressed by  $\alpha_{\text{em}}^2$  for the S-S type coupling and  $\alpha_{\text{em}}^2 v^2$  (where  $v \sim 10^{-3}$  is the DM velocity) for the P-S type coupling. In contrast, for pseudo-scalar and axial-vector lepton currents, i.e.  $\Gamma_\ell = \gamma_5, \gamma_\mu \gamma_5$ , the DM-nucleon coupling vanishes to all orders. Therefore, we have not shown the XENON1T and PANDAX-4T limits for the SP-type operator on the top left panel of Figure 5.

The same effective operator given in Eq. (2.1) also enables DM annihilation into electrons  $\chi\bar{\chi} \rightarrow e^+e^-$ . The exact analytic expressions for these cross sections in our EFT framework can be found in Appendix C of Ref. [85] for all the operator types. Using these, we calculate the thermal-averaged cross section times relative velocity  $\langle\sigma v\rangle$  which goes as  $m_\chi^2/\Lambda^4$  and compare it with the existing indirect detection upper limits on  $\langle\sigma v\rangle$  in the  $e^+e^-$  channel to put a lower bound on  $\Lambda$  as a function of the DM mass. This is shown in Figure 5 by the red and brown-shaded regions respectively for the Fermi-LAT [140] and AMS-02 [106] constraints on  $\langle\sigma v\rangle$ . Similar constraints on  $\langle\sigma v\rangle$  can be derived using CMB anisotropies [140], which is shown by the cyan-shaded region in Figure 5, assuming an  $s$ -wave annihilation (for  $p$ -wave annihilation, the CMB bound will be much weaker).

Along the dot-dashed line in Figure 5, the observed relic density can be reproduced for a WIMP DM. In principle, the region to the left and above of this line is disfavored for a thermal WIMP, because in this region  $\langle\sigma v\rangle$  is smaller than the observed value of  $\sim (2-5) \times 10^{-26} \text{ cm}^3 \text{ sec}^{-1}$  (depending on the DM mass [141]), which leads to an overabundance

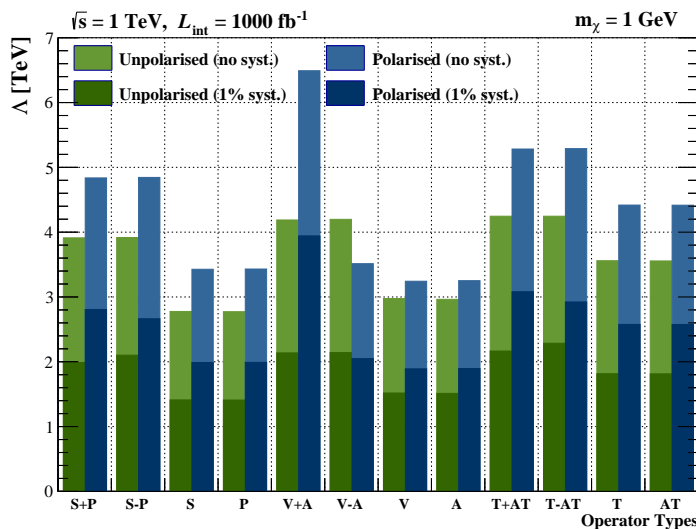


**Figure 6:**  $3\sigma$  sensitivity reach of different operators in the mono-photon channel with DM mass of 1 GeV at  $\sqrt{s} = 1$  TeV and  $\mathcal{L}_{\text{int}} = 1000 \text{ fb}^{-1}$ . The green (blue) bars show the sensitivity with unpolarized (polarized) beams and the lighter (darker) shade corresponds to zero (1%) background systematics.

of DM, since  $\Omega_\chi h^2 \propto 1/\langle\sigma v\rangle$ . However, this problem can be circumvented by either opening up additional leptonic annihilation channels (like  $\mu^+\mu^-$ ,  $\tau^+\tau^-$  and  $\nu\bar{\nu}$ ) or even going beyond the WIMP paradigm and invoking e.g., the freeze-in mechanism [142]. This will not affect the main results of our paper, since the collider phenomenology discussed here only depends on the DM coupling to electrons.

Also shown in Figure 5 is the supernova constraint, which excludes the magenta-shaded region from consideration of energy-loss and optical depth criteria from the observation of SN1987A [85]. Here we have used an average supernova core temperature of 30 MeV. Note that the supernova bound is only applicable for DM mass below  $\sim 200$  MeV or so, and for a certain range of  $\Lambda$  values, above which the DM particles cannot be efficiently produced in the supernova core, and below which they will no longer free-stream.

From Figure 5, we find that in spite of a large irreducible background, the accessible range of the cut-off scale  $\Lambda$  at  $\sqrt{s} = 1$  TeV ILC looks quite promising in the mono-photon channel, especially for low mass DM, where the collider sensitivity is almost flat, whereas the existing direct and indirect detection constraints are much weaker. This complementarity makes the collider searches for DM very promising. With unpolarized beams, the  $3\sigma$ -reach for the SP-type operator can be up to 3.9 TeV, while for the VA and TAT-type operators, it can be up to 4.2 TeV. With optimally polarized beams, i.e. with (+80%, +30%) for the SP and TAT-types and (+80%, -30%) for the VA type, the sensitivity reaches can be extended to 4.8 TeV (SP), 6.5 TeV (VA) and 5.3 TeV (TAT), as shown in Figure 5.

Now that we have the results for the SP, VA and TAT-type assuming all the relevant coefficients in Eq. (2.2) to be unity, it is instructive to see how the sensitivity reach differs for other choices of the coefficients. This is shown in Figure 6 for a fixed DM mass of 1 GeV.

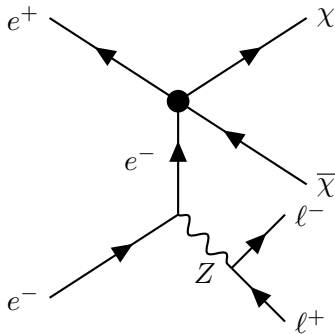


**Figure 7:** Feynman diagram for the leptonic mono- $Z$  channel. The  $Z$ -boson can also be emitted from the positron leg.

The green (blue) bars show the  $3\sigma$  ILC sensitivity with unpolarized (optimally polarized) beams and the lighter (darker) shade corresponds to zero (1%) background systematics. Here  $S+P$ ,  $V+A$  and  $T+AT$  refer to our default choice with all relevant coefficients equal to one, whereas  $S-P$  refers to the case with  $c_S^\chi = c_S^e = 1$  and  $c_P^\chi = c_P^e = -1$  (similarly for  $V-A$  and  $T-AT$ ), whereas pure  $S$ -type ( $P$ -type) means the pseudo-scalar (scalar) coefficients are zero (and similarly for pure vector, axial-vector, tensor and axial-tensor cases). We see that with the unpolarized beams, the best sensitivity is obtained for the  $T \pm AT$  operators, while with the polarized beams, the  $V+A$  operator gives the best sensitivity. In any case, all the operator types can be probed up to multi-TeV cut-off scales at  $\sqrt{s} = 1$  TeV with  $\mathcal{L}_{\text{int}} = 1000 \text{ fb}^{-1}$  integrated luminosity.

## 4 Mono- $Z$ channel

In addition to the mono-photon channel discussed in the previous section, another useful channel for leptophilic DM search at lepton colliders is the mono- $Z$  channel, where the  $Z$ -boson is emitted from one of the initial states. Depending on the subsequent decay of the  $Z$ -boson to either leptonic or hadronic final states, we perform a cut-based signal and background analysis, as discussed below.

### 4.1 Leptonic mode

For the leptonic decay of the  $Z$ -boson, we examine the process  $e^+e^- \rightarrow \chi\bar{\chi}Z(\rightarrow \ell^-\ell^+)$ , as shown in Figure 7. We will only consider  $\ell = e, \mu$  for simplicity and use the lepton pair as the visible particles for tagging. The main SM background for this channel is  $e^+e^- \rightarrow \nu\bar{\nu}\ell^+\ell^-$ , and it is polarization-dependent.

#### 4.1.1 Unpolarized and polarized cross-sections

For the signal and background simulation, we generated the UFO library for our EFT framework using `FeynRules` [132] and then generated events for both signal and background using `MadGraph 5` [143] with the following basic baseline cuts to the parameter space:

$$P_T(\ell) > 10 \text{ GeV}, \quad |\eta_\ell| \leq 2.5, \quad \Delta R_{\ell\ell} \geq 0.4. \quad (4.1)$$

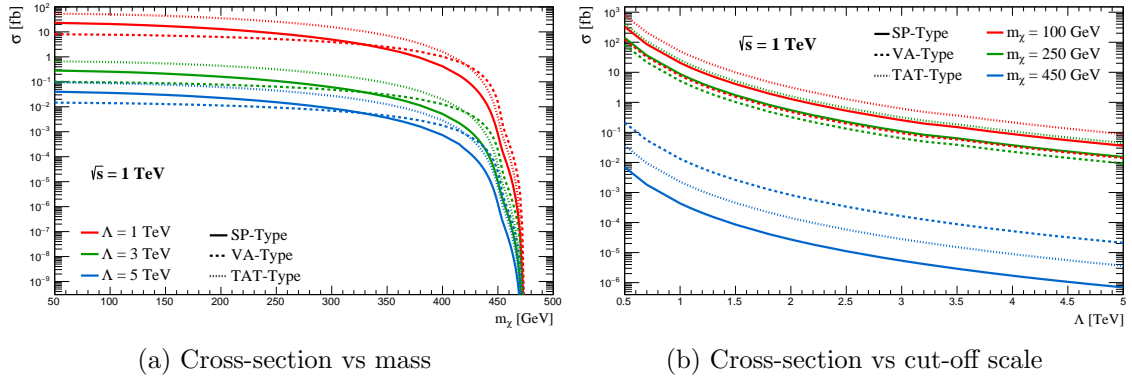


**Figure 8:** Variation of the mono- $Z$  leptonic cross-section with the DM mass (left panel) and cut-off scale (right panel) at  $\sqrt{s} = 1$  TeV ILC. The solid, dashed and dotted lines are for the SP, VA and TAT-type operators respectively. In the left panel, the red, green and blue curves correspond to different values of the cut-off scale  $\Lambda = 1$  TeV, 3 TeV and 5 TeV respectively, while in the right panel, they correspond to different values of the DM mass  $m_\chi = 100$  GeV, 250 GeV and 450 GeV respectively.

For the signal, the  $Z$ -bosons are decayed into the charged lepton pairs via the `MadSpin` [144, 145] package which is implemented in `MadGraph 5`, to take care of the spin-correlation effects of the lepton pairs. A fast detector simulation to these events is done using `Delphes 3` [135] with the same configuration card [136] as discussed in Section 3.1.

The variations of the signal cross section as a function of the DM mass and the cut-off scale are shown in Figure 8 left and right panels respectively for all three operator types, namely, SP (solid), VA (dashed) and TAT (dotted)-type. We find that the unpolarized cross-section is the smallest (largest) for the VA (TAT)-type operator at any given DM mass. In the left panel, the cross-section drops rapidly as  $m_\chi$  approaches  $\sqrt{s}/2 - m_Z$  due to phase-space suppression. Otherwise, for smaller DM masses, the cross-section for a given operator type and a given cut-off scale is almost independent of the DM mass, like in the mono-photon case (cf. Figure 3). In the right panel, we see that for a given DM mass the cross-section drops as  $\Lambda^{-4}$ , as expected.

With unpolarized beams, we find that the neutrino background cross section at  $\sqrt{s} = 1$  TeV is 420.5 fb, whereas the DM signal cross section is much smaller, as shown in Table 6 for a benchmark DM mass of  $m_\chi = 100$  GeV and the cut-off scale  $\Lambda = 3$  TeV.

Similar to the mono-photon case, we also examine the effect of polarization on the signal and background cross-sections, as shown in Table 6. The neutrino background can be reduced to 28% of its original value by making the electron beam +80% polarized, and further reduced to 21% of its original value by additionally making the positron beam -30% polarized. The (+80%, -30%) polarization configuration also enhances the VA-type signal by a factor of 2.4. However, the (+80%, +30%) configuration is better for the SP and TAT-type signals. For ease of comparison between different operator types, we choose to work with the (+80%, +30%) configuration democratically for all operator types, as well as for the background, unless otherwise specified.

Process type	Unpolarized cross-section (fb)	Polarization $P(e^-, e^+)$	Polarized cross-section (fb)			
			(+, +)	(+, -)	(-, +)	(-, -)
$\nu\bar{\nu}\ell^-\ell^+$	420	(80, 0)	116	116	723	723
		(80, 20)	135	98	856	590
		(80, 30)	145	88	926	523
SP-Type	0.28	(80, 0)	0.26	0.26	0.25	0.25
		(80, 20)	0.29	0.22	0.21	0.29
		(80, 30)	<b>0.32</b>	0.19	0.19	0.32
VA-Type	0.08	(80, 0)	0.15	0.15	0.02	0.02
		(80, 20)	0.12	0.18	0.01	0.02
		(80, 30)	0.11	<b>0.19</b>	0.01	0.02
TAT-Type	0.68	(80, 0)	0.62	0.62	0.62	0.62
		(80, 20)	0.72	0.52	0.52	0.72
		(80, 30)	<b>0.77</b>	0.47	0.47	0.77

**Table 6:** Comparison of the leptonic mono- $Z$  background and signal cross-sections for different choices of beam polarization for  $m_\chi = 100$  GeV and  $\Lambda = 3$  TeV at  $\sqrt{s} = 1$  TeV ILC. The numbers in bold highlight the optimal polarization choice for a given operator type.

#### 4.1.2 Cut-based analysis

Now we proceed with our cut-based analysis to enhance the signal-to-background ratio.

**Baseline selection cuts:** We define our signals by those events that pass through the baseline selection criteria as defined below where the  $Z$ -boson is reconstructed by the condition that all final state lepton-pairs are oppositely charged and of same flavor (OSSF).

$$P_{T,\ell} > 20 \text{ GeV}, \quad |\eta_\ell| < 2.45. \quad (4.2)$$

Other selection criteria are dynamic with respect to different BPs, as defined in Table 7. We have taken the same three BPs as in the mono-photon case to probe different regions of the parameter space, namely, BP1 essentially represents all light DM region, BP3 represents the region close to the kinematic limit of  $\sqrt{s}/2 - m_Z$ , whereas BP2 captures the intermediate DM mass region.

After implementing the baseline selection cuts given in Eq. (4.2), the signal and background cross sections are given (in parentheses) in the first rows of Tables 8 and 9 respectively. We find that the background is reduced to about 40% of its original value in Table 6 for the unpolarized (polarized) case, whereas the signals are reduced to about 60%-70% of their original values.

We now consider various kinematic distributions for the signal and background, as shown in Figure 9 for the unpolarized case (and Figure 18 in the Appendix for the polarized case). Based on these histograms, some specialized selection cuts are chosen as follows (also summarized in Table 7) which enhance the signal significance:

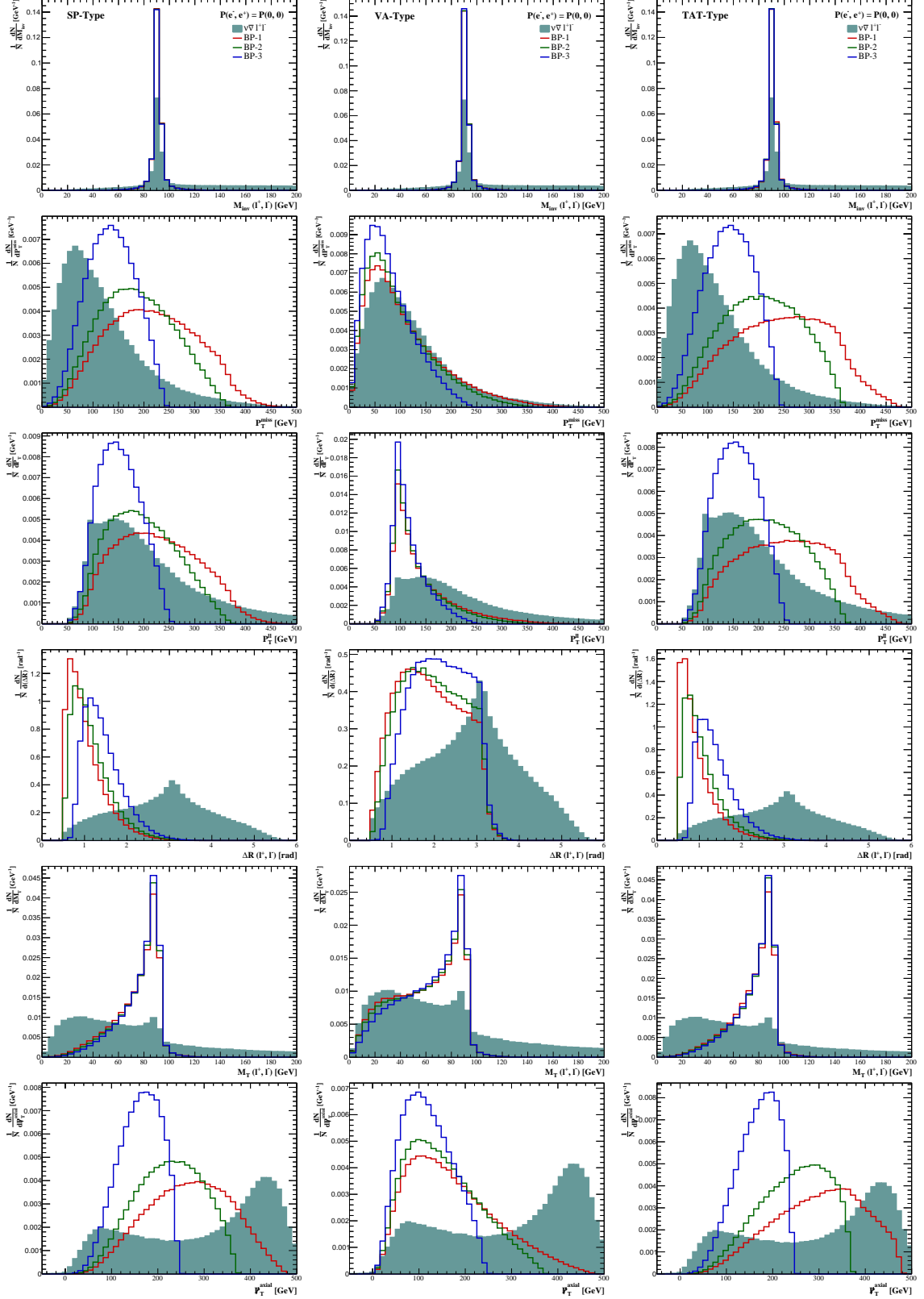


**Figure 9:** Normalized differential distributions for leptonic mono- $Z$  background (shaded) and signals after baseline selection cuts for the kinematic variables shown in Table 7 with unpolarized beams. The corresponding distributions with polarized beams are given in Figure 18 in the Appendix.

	BP1	BP2	BP3
<b>Definition</b>	$m_\chi = 100 \text{ GeV},$ $\Lambda = 3 \text{ TeV}$	$m_\chi = 250 \text{ GeV},$ $\Lambda = 3 \text{ TeV}$	$m_\chi = 350 \text{ GeV},$ $\Lambda = 3 \text{ TeV}$
Baseline selection	OSSF lepton-pairs with $P_{T,\ell} > 20 \text{ GeV},  \eta_\ell  < 2.45$		
<b>SP-type</b>			
Cut-1	$70 \text{ GeV} \leq M_{\text{inv}}(\ell^-\ell^+) \leq 110 \text{ GeV}$		
Cut-2	$160 \text{ GeV} < \cancel{E}_T$	$115 \text{ GeV} < \cancel{E}_T < 350 \text{ GeV}$	$100 \text{ GeV} < \cancel{E}_T < 230 \text{ GeV}$
Cut-3	$\Delta\eta_{\ell\ell} < 1.35, \Delta\phi_{\ell\ell} < 1.3 \text{ rad}$		
Cut-4	$M_T(\ell^-\ell^+) > 60 \text{ GeV}$		
Cut-5	$100 \text{ GeV} < \cancel{p}_T^{\text{axial}} < 435 \text{ GeV}$	$115 \text{ GeV} < \cancel{p}_T^{\text{axial}} < 350 \text{ GeV}$	$100 \text{ GeV} < \cancel{p}_T^{\text{axial}} < 230 \text{ GeV}$
<b>VA-type</b>			
Cut-1	$70 \text{ GeV} \leq M_{\text{inv}}(\ell^-\ell^+) \leq 110 \text{ GeV}$		
Cut-2	$P_T^{\ell\ell} < 360 \text{ GeV}$	$P_T^{\ell\ell} < 270 \text{ GeV}$	$P_T^{\ell\ell} < 215 \text{ GeV}$
Cut-3	$\Delta\eta_{\ell\ell} < 1.2, \Delta\phi_{\ell\ell} < 2.6 \text{ rad}$		
Cut-4	$M_T(\ell^-\ell^+) > 35 \text{ GeV}$		
Cut-5	$60 \text{ GeV} < \cancel{p}_T^{\text{axial}} < 380 \text{ GeV}$	$60 \text{ GeV} < \cancel{p}_T^{\text{axial}} < 290 \text{ GeV}$	$60 \text{ GeV} < \cancel{p}_T^{\text{axial}} < 220 \text{ GeV}$
<b>TAT-type</b>			
Cut-1	$70 \text{ GeV} \leq M_{\text{inv}}(\ell^-\ell^+) \leq 110 \text{ GeV}$		
Cut-2	$210 \text{ GeV} < \cancel{E}_T$	$165 \text{ GeV} < \cancel{E}_T < 360 \text{ GeV}$	$110 \text{ GeV} < \cancel{E}_T < 230 \text{ GeV}$
Cut-3	$\Delta\eta_{\ell\ell} < 1.2, \Delta\phi_{\ell\ell} < 1.2 \text{ rad}$		
Cut-4	$M_T(\ell^-\ell^+) > 60 \text{ GeV}$		
Cut-5	$100 \text{ GeV} < \cancel{p}_T^{\text{axial}} < 475 \text{ GeV}$	$100 \text{ GeV} < \cancel{p}_T^{\text{axial}} < 370 \text{ GeV}$	$100 \text{ GeV} < \cancel{p}_T^{\text{axial}} < 240 \text{ GeV}$

**Table 7:** Leptonic mono- $Z$  selection cuts for different BPs across operator types.

**Cut-1:** For the  $\nu\bar{\nu}\ell^-\ell^+$  background, the lepton pairs could come from different channels (such as from the  $t$ -channel  $W$  and  $Z$ -boson exchange, in addition to the on/off-shell  $WW$  and  $ZZ$  decays), the invariant mass of the lepton pairs are distributed over a wide range. But for the signals, the lepton pairs come as decay products of the on-shell  $Z$ -boson giving a sharp peak at the  $Z$ -boson mass, as is evident in Figure 9 (top row). Thus, selecting events that fall within a narrow window of dilepton invariant mass around the  $Z$ -mass, i.e.  $M_{\text{inv}}(\ell^+\ell^-) \in [70 \text{ GeV}, 110 \text{ GeV}]$ , suppresses the background significantly (to 28% of the baseline value with the unpolarized beams and to 23% with polarized beams, cf. Table 9) without affecting the signals much (cf. Table 8).

**Cut-2:** For smaller DM masses, the missing transverse momentum ( $P_T^{\text{miss}}$ ) tends to be harder than the neutrino background, so the signal distribution is to the right of the background. However, as the DM mass increases, the  $P_T^{\text{miss}}$  distribution peak shifts to the softer region, although it will have a sharper cut-off compared to the long-tail of the background. So we use a dynamic cut prescription across the three BPs and across the operators cf. Table 9). But as can be seen from Figure 9 (second row), the VA-type operator has very similar  $P_T^{\text{miss}}$  distribution as the background, and therefore, the  $P_T^{\text{miss}}$  cut is not very efficient in this case. So we chose to use another variable, namely, the  $P_T$ -sum of the lepton-pair  $P_T^{\ell\ell}$ , cf. Figure 9 (third row).

**Cut-3:** The lepton pairs coming from the  $Z$ -boson decay are expected to be more collinear than the ones in the background, as shown in Figure 9 (fourth row). So a strong upper



Selection cuts	Cut efficiencies					
	Unpolarized beams			Polarized beams		
	BP-1	BP-2	BP-3	BP-1	BP-2	BP-3
<b>SP-type:</b>						
Baseline selection	100% (0.20 fb)	100% (0.09 fb)	100% (0.02 fb)	100% (0.25 fb)	100% (0.12 fb)	100% (0.03 fb)
Cut-1	98.01%	97.73%	100%	98.39%	98.17%	96.00%
Cut-2	70.65%	79.55%	73.68%	70.56%	79.82%	72.00%
Cut-3	69.65%	73.86%	57.89%	69.76%	74.31%	56.00%
Cut-4	62.69%	67.05%	52.63%	62.90%	66.97%	52.00%
Cut-5	61.69%	65.91%	52.63%	61.69%	66.06%	48.00%
<b>VA-type:</b>						
Baseline selection	100% (0.05 fb)	100% (0.04 fb)	100% (0.02 fb)	100% (0.07 fb)	100% (0.05 fb)	100% (0.02 fb)
Cut-1	98.11%	100%	100%	98.48%	97.78%	95.45%
Cut-2	98.11%	97.14%	100%	98.48%	95.56%	95.45%
Cut-3	69.81%	68.57%	64.71%	71.21%	66.67%	63.64%
Cut-4	60.38%	60.00%	58.82%	60.61%	57.78%	54.55%
Cut-5	56.60%	54.29%	52.94%	57.58%	53.33%	50.00%
<b>TAT-type:</b>						
Baseline selection	100% (0.45 fb)	100% (0.26 fb)	100% (0.07 fb)	100% (0.56 fb)	100% (0.32 fb)	100% (0.09 fb)
Cut-1	98.23%	98.08%	98.59%	98.22%	98.14%	97.73%
Cut-2	62.39%	66.15%	69.01%	62.39%	66.25%	69.32%
Cut-3	62.17%	64.62%	49.30%	62.03%	64.71%	50.00%
Cut-4	58.19%	61.15%	47.89%	58.29%	61.30%	47.73%
Cut-5	58.19%	61.15%	47.89%	58.11%	61.30%	47.73%

**Table 8:** Cut-flow table for different operators and BPs for the leptonic mono- $Z$  signal. The cut efficiencies are calculated with respect to the baseline selection cuts given in Eq. (4.2), with the corresponding cross-sections shown (in parentheses) in the first row.

bound on  $\Delta R = \sqrt{(\Delta\eta)^2 + (\Delta\phi)^2}$  of the two leptons (where  $\Delta\eta$  and  $\Delta\phi$  are respectively the differences between the pseudorapidities and the azimuthal angles of the lepton-pairs) should be a good choice [146] to control the background. But here we do not put cuts on the  $\Delta R_{\ell\ell}$  variable directly, rather we choose to restrict  $\Delta\eta_{\ell\ell}$  and  $\Delta\phi_{\ell\ell}$  separately (cf. Table 7) that constitute  $\Delta R$ . This choice is stricter and turns out to be more efficient with respect to the signal significance than applying the  $\Delta R$  cut directly.

**Cut-4:** Next we consider the transverse mass ( $M_T$ ) of the reconstructed  $Z$ -boson, defined as  $M_T = \sqrt{(E_{T_1} + E_{T_2})^2 - (p_{x_1} + p_{x_2})^2 - (p_{y_1} + p_{y_2})^2}$ , where the suffixes 1 and 2 denote the hardest and second-hardest leptons in the final state, respectively. These distributions in Figure 9 (fifth row) look promising for separating the signal from background, if we apply a lower  $M_T$  cut. But for the VA-type it is found to be more spread in the softer region than the SP- or TAT-type; hence, a softer lower cut is used for the VA-type in Table 7. We did

Selection cuts	Cut efficiencies					
	Unpolarized beams			Polarized beams		
	BP-1	BP-2	BP-3	BP-1	BP-2	BP-3
Baseline selection	100% (169 fb)			100% (59 fb)		
<b>SP-type:</b>						
Cut-1	27.71%	27.71%	27.71%	23.11%	23.11%	23.11%
Cut-2	5.65%	9.80%	10.02%	4.80%	8.05%	8.12%
Cut-3	5.32%	7.71%	6.36%	4.54%	6.37%	5.16%
Cut-4	3.53%	4.51%	3.32%	2.86%	3.47%	2.51%
Cut-5	3.20%	4.08%	2.67%	2.45%	3.11%	1.99%
<b>VA-type:</b>						
Cut-1	27.71%	27.71%	27.71%	23.11%	23.11%	23.11%
Cut-2	27.42%	26.48%	25.05%	22.79%	21.94%	20.73%
Cut-3	18.36%	17.41%	16.01%	15.35%	14.49%	13.30%
Cut-4	13.24%	12.29%	10.89%	10.31%	9.45%	8.27%
Cut-5	11.22%	9.66%	7.70%	8.48%	7.24%	5.74%
<b>TAT-type:</b>						
Cut-1	27.71%	27.71%	27.71%	23.11%	23.11%	23.11%
Cut-2	2.90%	5.01%	8.60%	2.58%	4.18%	6.99%
Cut-3	2.80%	4.49%	4.82%	2.50%	3.76%	3.92%
Cut-4	2.12%	2.96%	2.60%	1.78%	2.30%	1.99%
Cut-5	1.89%	2.61%	2.14%	1.49%	1.99%	1.63%

**Table 9:** Cut-flow table for different operators and BPs for the leptonic mono- $Z$  background. The cut efficiencies are calculated with respect to the baseline selection cuts given in Eq. (4.2), with the corresponding cross-sections shown (in parentheses) in the first row. The background cut efficiencies vary across operator types because of the dynamic nature of the cuts chosen (cf. Table 7).

not apply a upper-cut here although it seems sensitive from the distributions in Figure 9, because after the application of the cut-1 (on  $M_{\text{inv}}$ ) the region above the upper-cut value diminishes for  $M_T$  also.

**Cut-5:** The final selection cut is applied on the variable  $\not{P}_T^{\text{axial}} = -\vec{\not{P}}_T \cdot \vec{P}^Z / P_T^Z$  [147]. This kind of variable is also used in other mono- $Z$  studies at the LHC [148, 149]. This variable turns out to be very efficient because of the tendency of the neutrinos (missing particles in the background) to have non-negligible momentum along the longitudinal direction as compared to the signals with massive missing particle. This is illustrated in Figure 9 bottom row.

We also considered some other variables, e.g.  $|\not{P}_T - P_T^Z| / P_T^Z$  [147–150] and  $\cos\theta_{\ell\ell}^* \equiv \tanh\Delta\eta_{\ell\ell}/2$  [149, 151]. But we found that after the application of all the above-mentioned cuts these variables are no longer sensitive in further enhancing our signal significance.

In Table 8, we tabulate the efficiencies of cuts 1 through 5 for the three signal BPs across all operator types. Table 9 contains the corresponding cut efficiencies for the background.

Operator Type	Signal significance for $\mathcal{L}_{\text{int}} = 1000 \text{ fb}^{-1}$					
	Unpolarized beams			Polarized beams		
	BP-1	BP-2	BP-3	BP-1	BP-2	BP-3
SP-type	1.7 (1.3)	0.7 (0.5)	0.1 (0.1)	3.8 (3.6)	1.7 (1.5)	0.3 (0.3)
VA-type	0.2 (0.1)	0.1 (0.1)	0.1 (0.1)	0.5 (0.4)	0.4 (0.3)	0.2 (0.2)
TAT-type	4.5 (3.9)	2.4 (1.9)	0.6 (0.5)	9.4 (9.1)	5.4 (5.1)	1.3 (1.3)

**Table 10:** Signal significance in the mono- $Z$  leptonic channel at  $\sqrt{s} = 1 \text{ TeV}$  and  $\mathcal{L}_{\text{int}} = 1000 \text{ fb}^{-1}$  after implementing all the cuts mentioned in the text. The values in the parenthesis denote the significances with a 1% background systematic uncertainty.

We find that after applying cuts 1-5, we can still retain about 35%-45% of the signal, whereas the background is reduced to below percent level of the original values given in Table 6.

#### 4.1.3 Results

After implementing all these cuts, we calculate the final signal significance for the three BPs using Eq. (3.4). Our results are given in Table 10 for an integrated luminosity of  $\mathcal{L}_{\text{int}} = 1000 \text{ fb}^{-1}$ . We see that as we go higher up in the DM mass the signal significance drops. We also find that the best-performing operator type is the TAT-type, for which more than 97% of the background events are removed after all the selection cuts. For the signal we retain 58% – 61% of the events, although for BP3 only 48% remains. The SP-type operator also gives good results, where we retain 50% – 66% of the signal across BPs and polarization choices, while removing more than 96% of the background events. Even for VA-type we retain more than 50% of the signal events and are able to cut down the background event yields to 11%. We also notice the positive effect of the beam polarization by which we achieve an enhancement of signal significance by more than 2 times compared to the ones with unpolarized beams. For VA-type though the significance can be further increased for the polarized beam case by choosing the left-handed positron beams as is evident from Table 6.

Going beyond the three BPs, we now vary the DM mass and present the  $3\sigma$  sensitivity reach for this channel in Figure 10 for all the operators. The labels and shaded regions are the same as in the mono-photon case (cf. Figure 5). We see that the accessible range of the cut-off scale  $\Lambda$  for the unpolarized beams can reach up to 3.2 TeV for the TAT-type operator, whereas for the SP and VA-type, it can reach up to 2.6 TeV and 1.6 TeV respectively. But with the application of optimally polarized beams as discussed earlier, we see an increase by about 25% of the  $3\sigma$  reach on the  $\Lambda$  scale, up to 3.2 TeV, 2.5 TeV and 4 TeV for the for SP, VA and TAT-type operators, respectively.

We also compare the leptonic mono- $Z$  sensitivities for different operator types in Figure 11 for a fixed DM mass of 1 GeV. As in Figure 6 for the mono-photon case, the green (blue) bars show the  $3\sigma$  sensitivity with unpolarized (polarized) beams and the lighter

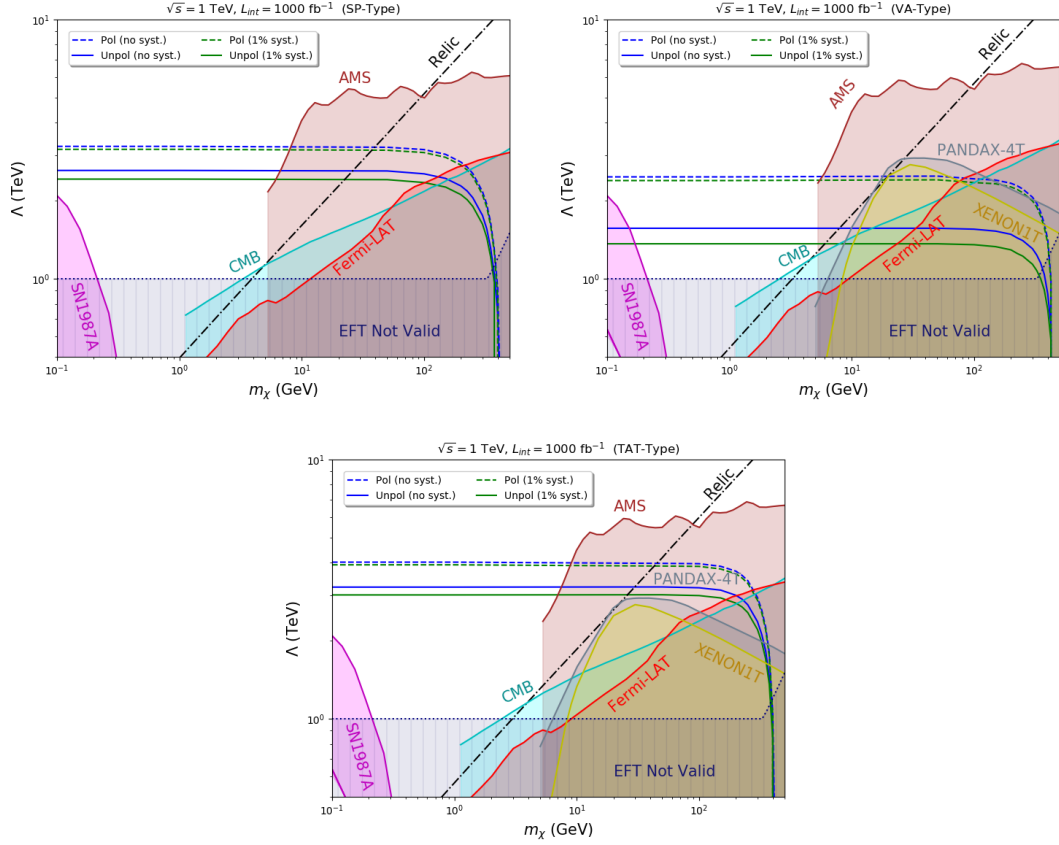


**Figure 10:**  $3\sigma$  sensitivity contours in the mono- $Z$  leptonic channel for the SP (top left panel), VA (top right panel) and TAT (bottom panel)-type operators with *unpolarized* (solid lines) and *polarized* (dashed lines)  $e^+e^-$  beams at  $\sqrt{s} = 1$  TeV center-of-mass energy and with  $\mathcal{L}_{\text{int}} = 1000 \text{ fb}^{-1}$  integrated luminosity. The blue (green) contours are assuming zero (1%) background systematics. The various shaded regions are excluded by direct detection (XENON1T, PANDAX-4T), indirect detection (Fermi-LAT, AMS), astrophysics (SN1987A) and cosmology (CMB) constraints. In the shaded region below  $\Lambda = \max\{\sqrt{s}/2, 3m_\chi\}$ , our EFT framework is not valid. Along the dot-dashed line, the observed DM relic density is reproduced for a thermal WIMP assuming only DM-electron effective coupling.

(darker) shade corresponds to zero (1%) background systematics. We again find the best sensitivity for  $T \pm AT$  operators, and the  $S \pm P$  operators also perform well, while the vector and axial-vector type operators have the weakest sensitivity in this channel, mainly because of its similarity to the background in the event distributions.

## 4.2 Hadronic mode

Now we look at the process  $e^+e^- \rightarrow \chi\bar{\chi}Z(\rightarrow jj)$ , where  $j \equiv u, d, c, s, b$  quarks (as shown in Figure 7). The relevant SM background processes for this channel are  $e^+e^- \rightarrow \nu\bar{\nu}jj$  and

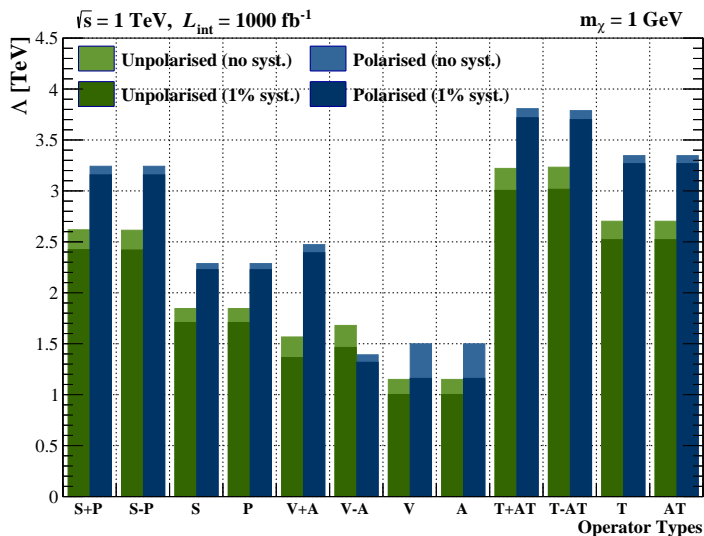


**Figure 11:**  $3\sigma$  sensitivity reach of different operators in the leptonic mono- $Z$  channel with DM mass of 1 GeV at  $\sqrt{s} = 1$  TeV and  $\mathcal{L}_{\text{int}} = 1000 \text{ fb}^{-1}$ . The green (blue) bars show the sensitivity with unpolarized (polarized) beams and the lighter (darker) shade corresponds to zero (1%) background systematics.

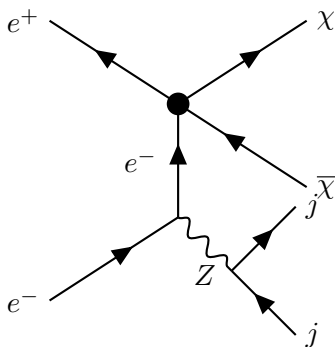


**Figure 12:** Feynman diagram for the hadronic mono- $Z$  channel. The  $Z$ -boson can also be emitted from the positron leg.

$e^+e^- \rightarrow jj\ell\nu$  (with one charged lepton escaping the detector) where the jets and leptons in the final state can come from any possible source (not necessarily from an on-shell  $Z$ ).

#### 4.2.1 Unpolarized and polarized cross-sections

We use the same UFO library as before which is implemented using `FeynRules` [132] and simulate the events for the signal and backgrounds via `MadGraph 5` [143] with the following basic cuts to the parameter space:

$$P_T(j, \ell) > 10 \text{ GeV}, \quad |\eta_j| \leq 3.0, \quad |\eta_\ell| \leq 2.5, \quad \Delta R_{jj, \ell j} \geq 0.4. \quad (4.3)$$

For the signals, as in the leptonic case, the on-shell  $Z$ -bosons are decayed into the pairs of jets using the `MadSpin` package [144, 145], implemented in `MadGraph 5`. Both the signal

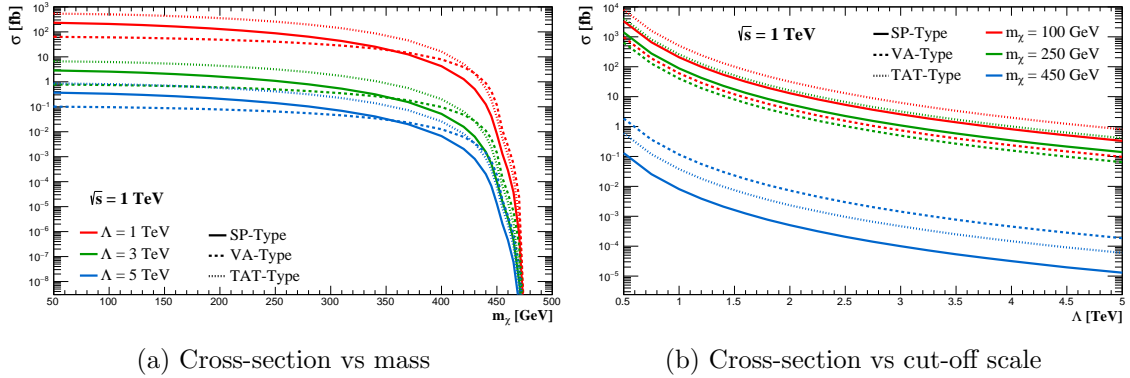


**Figure 13:** Variation of cross-section with DM mass (left panel) and cut-off scale (right panel) for the mono- $Z$  hadronic channel. The solid, dashed and dotted lines are for the SP, VA and TAT-type operators respectively. In the left panel, the red, green and blue curves correspond to different values of the cut-off scale  $\Lambda = 1$  TeV, 3 TeV and 5 TeV respectively, while in the right panel, they correspond to different values of the DM mass  $m_\chi = 100$  GeV, 250 GeV and 450 GeV respectively.

and background samples are hadronized using Pythia8.2 [152] and then the final state jets are reconstructed with with `anti- $k_T$`  [153] clustering algorithm with a minimum  $P_T$  of 10 GeV and a cone radius ( $R$ ) of 0.4 using the `FastJet` [154] package. The fast detector simulation to these events are done using `Delphes 3` [135] with the same configuration card [136] as discussed in Section 3.1.

With unpolarized beams, we find the neutrino-pair background is 798 fb, whereas the  $jj\ell\nu$  background is 1186 fb. On the other hand, the DM signal is only at a few fb level, as shown in Table 11 for a benchmark DM mass of  $m_\chi = 100$  GeV and the cut-off scale  $\Lambda = 3$  TeV. The variations of the signal cross section with the DM mass and cut-off scale are shown in Figure 13. We find the unpolarized cross section is the largest for the TAT-type operator, similar to the leptonic mono- $Z$  channel.

We then examine different choices of beam-polarization on both the event samples for this channel, as shown in Table 11. We find that both the backgrounds are polarization-dependent and fall off significantly for right-handed electron beam and with increasing degree of polarization. For this channel also we choose the polarization configuration  $P(e^-, e^+) = (+80\%, +30\%)$  democratically over all the operator types.

#### 4.2.2 Cut-based analysis

After obtaining the signal and background cross-sections as reported in Table 11, we proceed with our cut-based analysis to optimize the signal significance, as follows.

**Baseline selection cuts:** We select the events that contain at least two jets with the following transverse momentum and pseudorapidity requirements:

$$P_{T,j} > 20 \text{ GeV}, \quad |\eta_j| < 2.45. \quad (4.4)$$

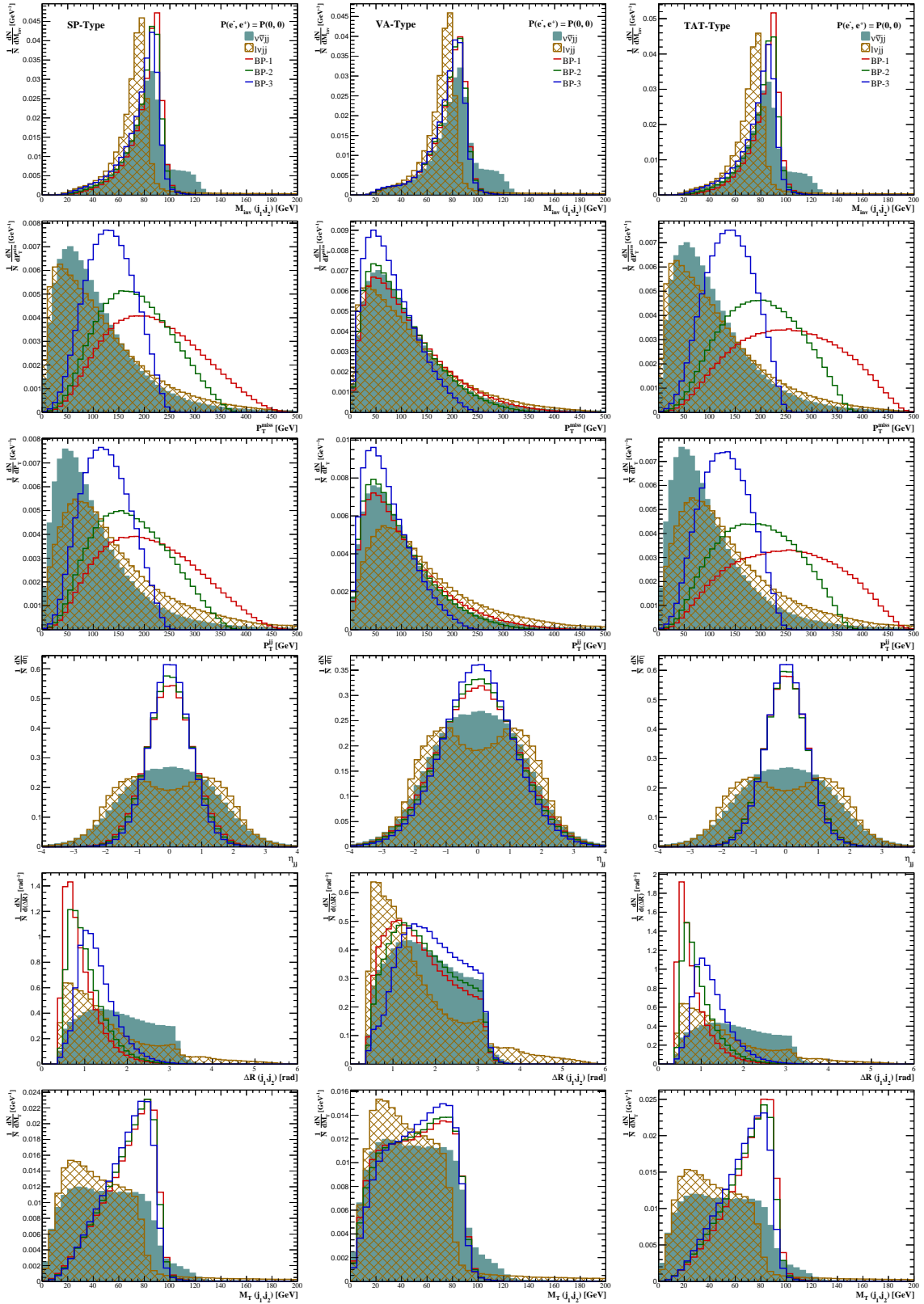
Process type	Unpolarized cross-section (fb)	Pol. $P(e^-, e^+)$	Polarized cross-section (fb)			
			(+, +)	(+, -)	(-, +)	(-, -)
$\nu\bar{\nu}jj$	798	(80, 0)	178	178	1415	1415
		(80, 20)	206	151	1689	1134
		(80, 30)	219	136	1833	989
$jj\ell\nu$	1186	(80, 0)	302	302	2061	2061
		(80, 20)	359	246	2446	1685
		(80, 30)	386	216	2635	1492
SP-Type	2.78	(80, 0)	2.57	2.57	2.58	2.58
		(80, 20)	2.98	2.15	2.15	2.97
		(80, 30)	<b>3.17</b>	1.95	1.95	3.17
VA-Type	0.83	(80, 0)	1.35	1.35	0.15	0.15
		(80, 20)	1.07	1.61	0.12	0.18
		(80, 30)	0.94	<b>1.76</b>	0.10	0.19
TAT-Type	6.77	(80, 0)	6.22	6.22	6.21	6.21
		(80, 20)	7.23	5.23	5.24	7.21
		(80, 30)	<b>7.72</b>	4.73	4.73	7.69

**Table 11:** Comparison of the hadronic mono- $Z$  background and signal cross-sections for different choices of beam polarization with  $m_\chi = 100$  GeV and  $\Lambda = 3$  TeV at  $\sqrt{s} = 1$  TeV ILC. The numbers in bold highlight the optimal polarization choice for a given operator type.

The hardest two jets are required to reconstruct the  $Z$ -boson. The signal and background cross-sections after implementing these cuts are given (in parentheses) in the first rows of Tables 13 and 14 respectively. Further selection cuts are applied some of which depend on the DM mass. So, as in the leptonic channel, we have taken the same three BPs with varying DM mass and impose dynamic cuts. The benchmark parameters and the different selection cuts are defined in Table 12.

**Cut-1:** The contribution to the  $\nu\bar{\nu}jj$  background comes mainly from the process  $e^+e^- \rightarrow Z + \gamma/Z$  where the dijet comes from the  $\gamma/Z$  boson, whereas the  $\ell\nu jj$  background comes largely from  $e^+e^- \rightarrow W^+W^-$ , followed by leptonic decay of one  $W$  and hadronic decay of the other  $W$ . So, by selecting a dijet invariant mass around the  $Z$  mass, i.e.  $85\text{GeV} \leq M_{\text{inv}}(jj) \leq 100\text{GeV}$ , the backgrounds are reduced considerably. In particular the  $\ell\nu jj$  background with a peak around the  $W$ -boson mass (see Figure 14 top row) is reduced by 96% whereas 72% of the  $\nu\bar{\nu}jj$  background is rejected (cf. Table 14).

**Cut-2:** As was the case for the leptonic channel, the missing transverse momentum ( $P_T^{\text{miss}}$ ) distribution for the signal depends on the DM mass. As the mass of the DM increases, the distribution of missing transverse momentum ( $P_T^{\text{miss}}$ ) becomes softer and dies out at lower values. So an upper limit on  $P_T^{\text{miss}}$  is effective in reducing the backgrounds. But as can be seen from the histograms in Figure 9 (second row), the VA-type operator is not sensitive to this missing  $P_T$  variable. So we use a cut on the  $P_T$  of the



(continued to next page)



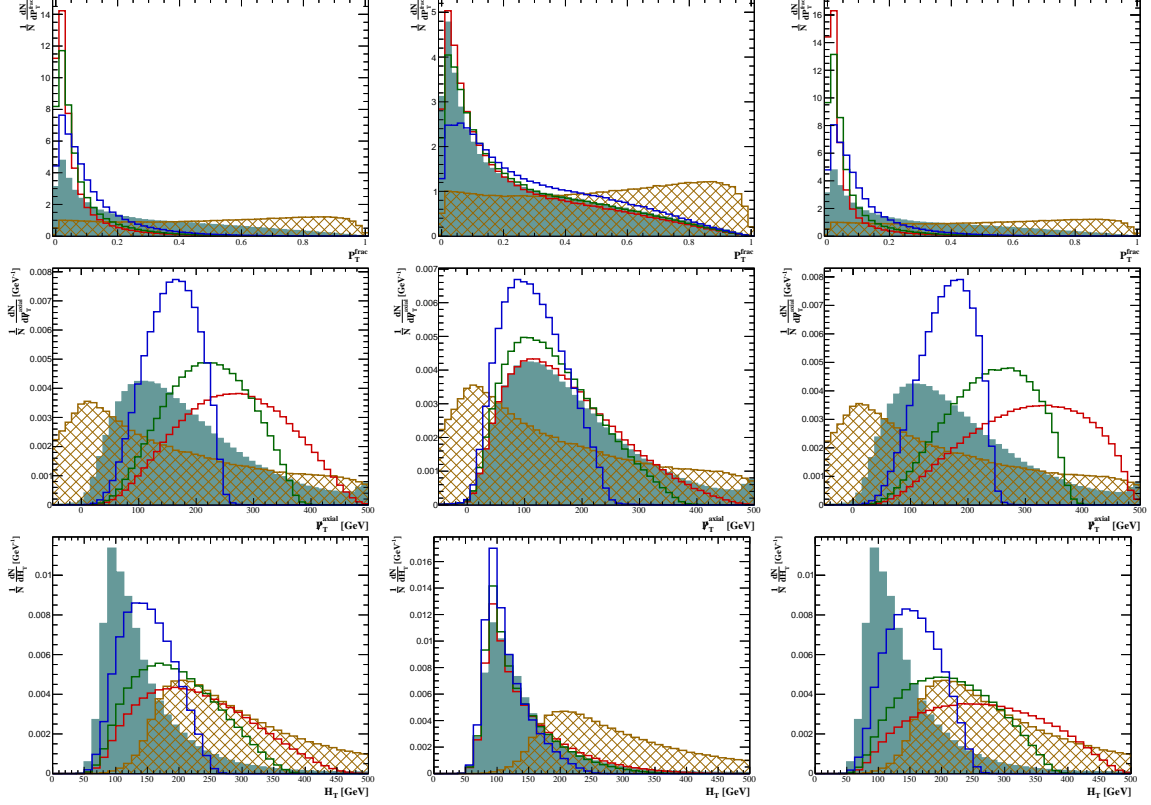


**Figure 14:** Normalized differential distributions for hadronic mono- $Z$  backgrounds (shaded) and signals after baseline selection cuts for the kinematic variables shown in Table 12 with unpolarized beams. The corresponding distributions for polarized beams are given in Figure 19 in the Appendix.

reconstructed  $Z$ -boson for the VA-type looking at the histograms in Figure 9 (third row), as shown in Table 12.

**Cut-3:** This is based on the pseudorapidity of the momentum-sum of the two jets. As evident from the distributions in Figure 15 (fourth row), the signal peaks in the transverse direction while the  $\nu\bar{\nu}jj$  background remains flat and  $\ell\nu jj$  tends to dip there. Hence, putting a cut on  $|\eta_j|$  reduces the background considerably.

**Cut-4:** We put a cut on  $\Delta R_{jj}$  to remove significant amount of events for both the backgrounds that are less collinear than the signals where the jets come from on-shell resonant decay of  $Z$ -boson, as discussed for the leptonic channel, and as shown in Figure 15 (fifth row).

**Cut-5:** The transverse mass ( $M_T$ ) distribution of the reconstructed  $Z$ -boson also looks promising for suppressing both the backgrounds, as shown in Figure 15 (sixth row). As in the leptonic channel the cut on  $M_{\text{inv}}$  deems the higher energy region insensitive for this selection cut.

	<b>BP1</b>	<b>BP2</b>	<b>BP3</b>
<b>Definition</b>	$m_\chi = 100 \text{ GeV},$ $\Lambda = 3 \text{ TeV}$	$m_\chi = 250 \text{ GeV},$ $\Lambda = 3 \text{ TeV}$	$m_\chi = 350 \text{ GeV},$ $\Lambda = 3 \text{ TeV}$
Baseline selection	$P_{T,j} > 20 \text{ GeV}, \quad  \eta_j  < 2.45$		
<b>SP-type</b>			
Cut-1	$85 \text{ GeV} \leq M_{\text{inv}}(jj) \leq 100 \text{ GeV}$		
Cut-2	$250 \text{ GeV} < \cancel{E}_T$	$200 \text{ GeV} < \cancel{E}_T < 330 \text{ GeV}$	$110 \text{ GeV} < \cancel{E}_T < 230 \text{ GeV}$
Cut-3	$ \eta_j  < 1.2$		
Cut-4	$ \Delta R_{jj}  < 1.5$		
Cut-5	$M_T(j_1 j_2) > 60 \text{ GeV}$		
Cut-6	$P_T^{\text{frac}} < 0.16$		
Cut-7	$250 \text{ GeV} < \cancel{P}_T^{\text{axial}} < 450 \text{ GeV}$	$220 \text{ GeV} < \cancel{P}_T^{\text{axial}} < 340 \text{ GeV}$	$110 \text{ GeV} < \cancel{P}_T^{\text{axial}} < 230 \text{ GeV}$
Cut-8	$H_T < 460 \text{ GeV}$	$H_T < 340 \text{ GeV}$	$H_T < 250 \text{ GeV}$
<b>VA-type</b>			
Cut-1	$84 \text{ GeV} \leq M_{\text{inv}}(jj) \leq 98 \text{ GeV}$		
Cut-2	$P_T^Z < 310 \text{ GeV}$	$P_T^Z < 280 \text{ GeV}$	$P_T^Z < 180 \text{ GeV}$
Cut-3	$ \eta_j  < 1.$		
Cut-4	$ \Delta R_{jj}  < 1.6$		
Cut-5	$M_T(j_1 j_2) > 55 \text{ GeV}$		
Cut-6	$P_T^{\text{frac}} < 0.2$		
Cut-7	$100 \text{ GeV} < \cancel{P}_T^{\text{axial}} < 400 \text{ GeV}$	$110 \text{ GeV} < \cancel{P}_T^{\text{axial}} < 300 \text{ GeV}$	$50 \text{ GeV} < \cancel{P}_T^{\text{axial}} < 240 \text{ GeV}$
Cut-8	$H_T < 330 \text{ GeV}$	$H_T < 290 \text{ GeV}$	$H_T < 210 \text{ GeV}$
<b>TAT-type</b>			
Cut-1	$85 \text{ GeV} \leq M_{\text{inv}}(jj) \leq 100 \text{ GeV}$		
Cut-2	$220 \text{ GeV} < \cancel{E}_T < 450 \text{ GeV}$	$180 \text{ GeV} < \cancel{E}_T < 370 \text{ GeV}$	$120 \text{ GeV} < \cancel{E}_T < 240 \text{ GeV}$
Cut-3	$ \eta_j  < 0.8$		
Cut-4	$ \Delta R_{jj}  < 1.5$		
Cut-5	$M_T(j_1 j_2) > 65 \text{ GeV}$		
Cut-6	$P_T^{\text{frac}} < 0.15$		
Cut-7	$280 \text{ GeV} < \cancel{P}_T^{\text{axial}} < 470 \text{ GeV}$	$220 \text{ GeV} < \cancel{P}_T^{\text{axial}} < 380 \text{ GeV}$	$140 \text{ GeV} < \cancel{P}_T^{\text{axial}} < 240 \text{ GeV}$
Cut-8	$H_T < 440 \text{ GeV}$	$H_T < 370 \text{ GeV}$	$H_T < 250 \text{ GeV}$

**Table 12:** Different BPs and selection cuts across operator types for mono-Z hadronic channel.

**Cut-6:** Next we consider the fractional  $P_T$  defined as  $P_T^{\text{frac}} = |\cancel{P}_T - P_T^Z|/P_T^Z$ . This variable gives an estimation of the momentum imbalance of the system. For the signal samples the reconstructed  $Z$ -bosons are more correlated to the missing energy due to the DM pair compared to the backgrounds which is spread all the way to  $P_T^{\text{frac}} \approx 1$ , as is evident from Figure 15 (seventh row).

**Cut-7:** The variable  $\cancel{P}_T^{\text{axial}} = -\vec{\cancel{P}}_T \cdot \vec{P}^Z / P_T^Z$  is also efficient in removing the backgrounds, in particular, the events of  $\ell\nu jj$  which peak at lower values, as shown in Figure 15 (eighth row). So cutting it from below removes majority of the background events. Also this variable, being a function of the missing  $P_T$ , depends on the DM mass, so we employ different cut-values across the BPs.

**Cut-8:** The final selection cut is on the scalar sum of the transverse energies ( $H_T$ ), whose distributions are shown in Figure 15 (bottom row). This removes the  $\nu\bar{\nu}jj$  background

Selection cuts	Cut efficiencies					
	Unpolarized beams			Polarized beams		
	BP-1	BP-2	BP-3	BP-1	BP-2	BP-3
<b>SP-type:</b>						
Baseline selection	100% (2.41 fb)	100% (1.01 fb)	100% (0.22 fb)	100% (2.99 fb)	100% (1.25 fb)	100% (0.28 fb)
Cut-1	45.32%	40.60%	32.31%	45.30%	40.57%	32.40%
Cut-2	22.49%	20.88%	24.86%	22.44%	20.83%	24.93%
Cut-3	22.48%	20.88%	24.68%	22.43%	20.82%	24.76%
Cut-4	22.48%	20.88%	23.08%	22.43%	20.82%	23.12%
Cut-5	22.03%	20.46%	22.18%	22.00%	20.41%	22.22%
Cut-6	22.03%	20.45%	21.46%	22.00%	20.40%	21.49%
Cut-7	21.42%	17.84%	20.16%	21.38%	17.84%	20.18%
Cut-8	21.42%	17.81%	20.16%	21.38%	17.82%	20.18%
<b>VA-type:</b>						
Baseline selection	100% (0.69 fb)	100% (0.46 fb)	100% (0.22 fb)	100% (0.18 fb)	100% (0.12 fb)	100% (0.06 fb)
Cut-1	33.32%	31.89%	29.02%	33.42%	32.04%	29.33%
Cut-2	31.64%	30.64%	26.91%	31.74%	30.83%	27.21%
Cut-3	19.18%	19.14%	17.17%	19.21%	19.30%	17.37%
Cut-4	13.53%	12.66%	8.16%	13.56%	12.72%	8.26%
Cut-5	13.53%	12.65%	8.16%	13.55%	12.72%	8.26%
Cut-6	13.07%	12.12%	7.47%	13.08%	12.19%	7.55%
Cut-7	12.96%	11.39%	7.45%	12.98%	11.47%	7.53%
Cut-8	12.95%	11.33%	7.43%	12.97%	11.41%	7.51%
<b>TAT-type:</b>						
Baseline selection	100% (5.83 fb)	100% (2.99 fb)	100% (0.79 fb)	100% (7.23 fb)	100% (3.71 fb)	100% (0.98 fb)
Cut-1	49.64%	43.17%	33.31%	49.68%	43.17%	33.37%
Cut-2	36.28%	31.61%	25.26%	36.32%	31.60%	25.31%
Cut-3	32.25%	28.60%	22.94%	32.30%	28.58%	22.96%
Cut-4	32.25%	28.59%	22.23%	32.30%	28.57%	22.26%
Cut-5	32.20%	28.54%	22.18%	32.26%	28.52%	22.21%
Cut-6	32.20%	28.53%	21.70%	32.25%	28.51%	21.72%
Cut-7	27.33%	25.41%	20.15%	27.43%	25.39%	20.17%
Cut-8	26.37%	25.24%	20.06%	26.47%	25.22%	20.08%

**Table 13:** Cut-flow chart for different operators and BPs for the mono- $Z$  hadronic  $signal$  at  $\sqrt{s} = 1$  TeV and  $\mathcal{L}_{int} = 1000 \text{ fb}^{-1}$ . The cut efficiencies are calculated with respect to Eq. (4.4), with the corresponding cross-sections shown (in parentheses) in the first row.

mainly. After the application of this cut the  $\nu\bar{\nu}jj$  background is reduced to  $1 - 4\%$  of the yield after the baseline-selection cut whereas the  $\ell\nu jj$  events are reduced to  $0.01 - 0.1\%$ . Tables 13 and 14 display the efficiencies of the selection cuts on the signal and the two backgrounds considering the event yields after the baseline selection to be 100%.

Selection cuts	Cut efficiencies											
	Unpolarized beams						Polarized beams					
	$\nu_\ell \bar{\nu}_\ell jj$			$\ell \nu_\ell jj$			$\bar{\ell} \nu_\ell jj$			$\ell \nu_\ell jj$		
	BP-1	BP-2	BP-3	BP-1	BP-2	BP-3	BP-1	BP-2	BP-3	BP-1	BP-2	BP-3
BS	100% (532 fb)			100% (146 fb)			100% (775 fb)			100% (254 fb)		
<b>SP-type:</b>												
Cut-1	27.54%	27.54%	27.54%	3.79%	3.79%	3.79%	27.81%	27.81%	27.81%	3.68%	3.68%	3.68%
Cut-2	2.89%	4.32%	9.75%	0.53%	0.62%	1.18%	3.50%	4.60%	9.68%	0.50%	0.59%	1.11%
Cut-3	2.80%	3.93%	7.54%	0.50%	0.51%	0.76%	3.35%	3.97%	7.18%	0.46%	0.49%	0.68%
Cut-4	2.8%	3.92%	6.34%	0.46%	0.45%	0.59%	3.35%	3.96%	6.02%	0.42%	0.43%	0.54%
Cut-5	2.51%	3.37%	5.28%	0.40%	0.36%	0.46%	2.89%	3.27%	5.03%	0.36%	0.34%	0.44%
Cut-6	2.50%	3.35%	5.01%	0.16%	0.10%	0.08%	2.89%	3.26%	4.76%	0.16%	0.10%	0.07%
Cut-7	2.07%	2.56%	3.90%	0.09%	0.04%	0.04%	2.10%	2.46%	3.71%	0.09%	0.05%	0.03%
Cut-8	2.06%	2.55%	3.90%	0.06%	0.02%	0.01%	2.10%	2.45%	3.71%	0.07%	0.02%	0.01%
<b>VA-type:</b>												
BS	100%	100%	100%	100%	100%	100%	100%	100%	100%	100%	100%	100%
Cut-1	29.27%	29.27%	29.27%	4.66%	4.66%	4.66%	29.57%	29.57%	29.57%	4.53%	4.53%	4.53%
Cut-2	27.53%	26.88%	22.30%	3.54%	3.27%	2.13%	27.28%	26.51%	21.82%	3.54%	3.29%	2.19%
Cut-3	14.40%	13.85%	10.31%	1.40%	1.29%	0.79%	13.83%	13.27%	9.94%	1.45%	1.33%	0.80%
Cut-4	8.87%	8.32%	4.78%	1.08%	0.97%	0.47%	8.54%	7.98%	4.65%	1.15%	1.04%	0.50%
Cut-5	8.86%	8.32%	4.78%	1.08%	0.97%	0.47%	8.54%	7.98%	4.64%	1.15%	1.03%	0.50%
Cut-6	8.56%	8.02%	4.48%	0.26%	0.22%	0.09%	8.25%	7.69%	4.36%	0.26%	0.22%	0.08%
Cut-7	8.45%	7.25%	4.30%	0.17%	0.12%	0.06%	8.14%	6.95%	4.18%	0.17%	0.12%	0.05%
Cut-8	8.45%	7.22%	4.27%	0.09%	0.04%	0.00%	8.14%	6.93%	4.15%	0.10%	0.05%	0.00%
<b>TAT-type:</b>												
BS	100%	100%	100%	100%	100%	100%	100%	100%	100%	100%	100%	100%
Cut-1	27.54%	27.54%	27.54%	3.79%	3.79%	3.79%	27.81%	27.81%	27.81%	3.68%	3.68%	3.68%
Cut-2	4.17%	6.15%	8.99%	0.70%	0.89%	1.09%	4.83%	6.53%	8.94%	0.66%	0.82%	1.02%
Cut-3	3.03%	4.09%	5.06%	0.45%	0.49%	0.46%	3.26%	3.95%	4.82%	0.42%	0.45%	0.43%
Cut-4	3.03%	4.08%	4.54%	0.42%	0.43%	0.36%	3.26%	3.93%	4.33%	0.39%	0.40%	0.34%
Cut-5	3.02%	4.06%	4.53%	0.41%	0.42%	0.36%	3.25%	3.92%	4.31%	0.38%	0.39%	0.34%
Cut-6	3.01%	4.04%	4.33%	0.14%	0.10%	0.07%	3.24%	3.89%	4.11%	0.15%	0.11%	0.06%
Cut-7	1.85%	2.98%	3.41%	0.08%	0.05%	0.03%	1.90%	2.90%	3.24%	0.09%	0.06%	0.03%
Cut-8	1.83%	2.96%	3.39%	0.05%	0.03%	0.00%	1.87%	2.87%	3.23%	0.06%	0.03%	0.00%

**Table 14:** Cut-flow chart for different operators and BPs for the mono- $Z$  hadronic *backgrounds* at  $\sqrt{s} = 1$  TeV and  $\mathcal{L}_{\text{int}} = 1000 \text{ fb}^{-1}$ . The cut efficiencies are calculated with respect to Eq. (4.4), with the corresponding cross-sections shown (in parentheses) in the first row. The background cut efficiencies vary across operator types because of the dynamic nature of the cuts chosen (cf. Table 12).

### 4.2.3 Results

The signal significances calculated using Eq. (3.4) are tabulated in Table 15. We see similar behavior for the different BPs as in the previously discussed channels, i.e. enhanced signal significance with decreasing mass of the DM. The selection cuts are most efficient for SP- and TAT-type operators. For BP-1 we remove more than 98% of the background events while keeping at least 21% of the signal events for the two operator types, yielding a large signal significance especially for the TAT-type operator with polarized beams.

Varying the DM mass, we display the  $3\sigma$  sensitivity contours for all three operators in Figure 15. It is clear that the TAT-type operator has the best sensitivity, which reaches

Operator types	Signal significance for $\mathcal{L}_{\text{int}} = 1000 \text{ fb}^{-1}$					
	Unpolarized beams			Polarized Beam		
	BP-1	BP-2	BP-3	BP-1	BP-2	BP-3
SP-type	4.7 (3.3)	1.5 (1.0)	0.3 (0.2)	10.3 (9.1)	3.6 (3.1)	0.8 (0.6)
VA-type	0.4 (0.2)	0.3 (0.1)	0.1 (0.1)	0.2 (0.1)	0.1 (0.1)	0.1 (0.04)
TAT-type	14.2 (10.4)	5.8 (3.7)	1.2 (0.7)	27.7 (25.6)	12.9 (11.1)	2.8 (2.3)

**Table 15:** Signal significances of the mono- $Z$  hadronic channel at  $\sqrt{s} = 1 \text{ TeV}$  and  $\mathcal{L}_{\text{int}} = 1000 \text{ fb}^{-1}$  after implementing all analysis cuts mentioned in the text. The values in the parenthesis denote the significance with a 1% background systematic uncertainty.

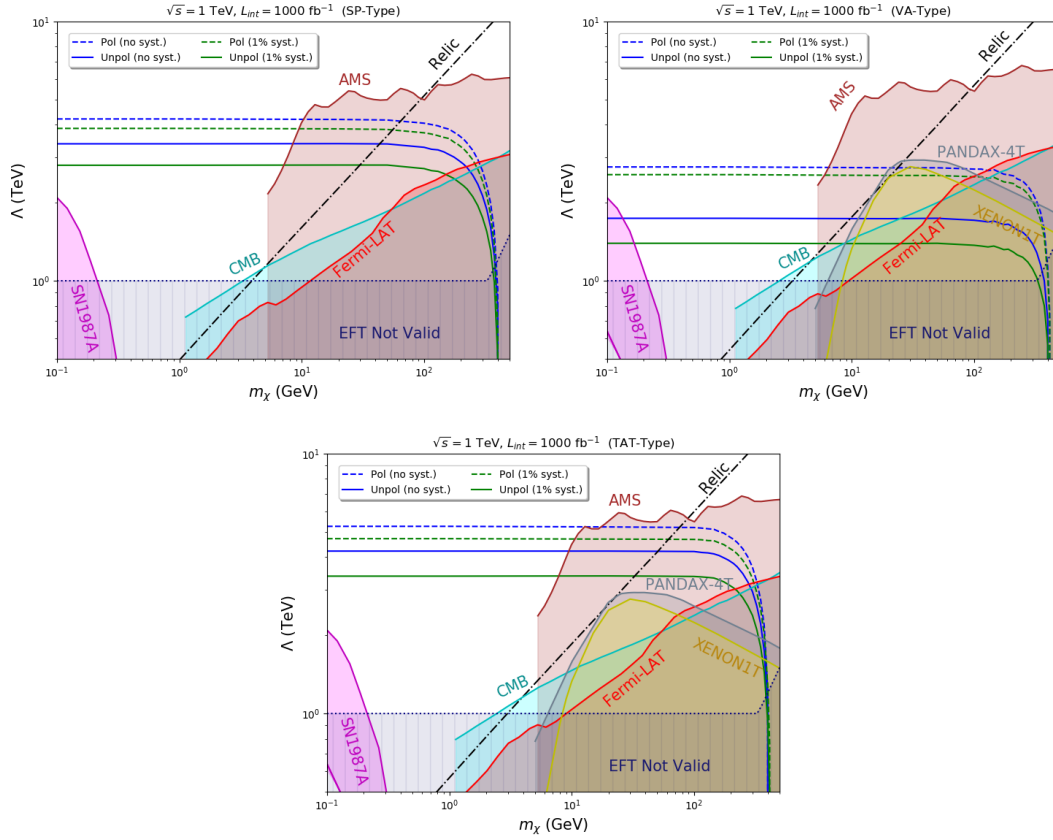


**Figure 15:**  $3\sigma$  sensitivity contours in the mono- $Z$  hadronic channel. The labels are the same as in Figure 10.

up to 4.2 TeV with unpolarized beams and 5.2 TeV with optimally polarized beams. The SP-type operator also has a sensitivity comparable to the mono-photon channel, and can reach up to 3.4 (4.2) TeV with unpolarized (polarized) beams. The VA-type operator has a modest sensitivity in this channel, only up to 1.7 (2.7) TeV with unpolarized (polarized) beams.

We also compare the hadronic mono- $Z$  sensitivities for different operator types in

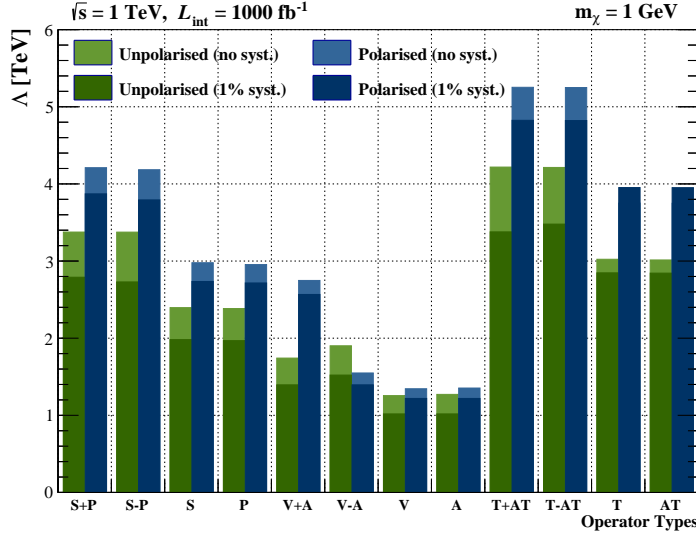


**Figure 16:**  $3\sigma$  sensitivity reach of different operators in the mono- $Z$  hadronic channel with DM mass of 1 GeV at  $\sqrt{s} = 1$  TeV and  $\mathcal{L}_{\text{int}} = 1000 \text{ fb}^{-1}$ . The green (blue) bars show the sensitivity with unpolarized (polarized) beams and the lighter (darker) shade corresponds to zero (1%) background systematics.

Process type	Beam configuration	$3\sigma$ sensitivity reach of $\Lambda$ (TeV)		
		SP	VA	TAT
Mono- $\gamma$	Unpolarized	3.91 (1.99)	4.19 (2.14)	4.25 (2.17)
	Polarized	<b>4.84</b> (2.81)	<b>6.49</b> ( <b>3.94</b> )	<b>5.28</b> (3.08)
Mono- $Z$ leptonic	Unpolarized	2.62 (2.42)	1.57 (1.36)	3.22 (3.00)
	Polarized	3.24 (3.16)	2.47 (2.39)	4.02 (3.93)
Mono- $Z$ hadronic	Unpolarized	3.38 (2.79)	1.74 (1.39)	4.22 (3.38)
	Polarized	4.21 ( <b>3.87</b> )	2.75 (2.57)	5.25 ( <b>4.71</b> )

**Table 16:** Summary of our results for the  $3\sigma$  sensitivity reach of the cut-off scale  $\Lambda$  in the three different channels discussed in the text. Here we have fixed the DM mass at 1 GeV. The numbers in parentheses are with 1% background systematics. The numbers in bold show the highest  $\Lambda$  value that can be probed for a given operator.

Figure 16 for a fixed DM mass of 1 GeV. The green (blue) bars show the  $3\sigma$  sensitivity with unpolarized (polarized) beams and the lighter (darker) shade corresponds to zero (1%) background systematics. We again find the best sensitivity for  $T \pm AT$  operators, followed by the  $S \pm P$  operators, while the vector and axial-vector type operators have the weakest sensitivity in this channel, mainly because of its similarity to the background in the event distributions, just as in the leptonic mono- $Z$  case. In general, the hadronic mono- $Z$  channel is more effective than the leptonic one, primarily because of a larger signal cross section due to higher hadronic branching ratio (69.9%) of the  $Z$ -boson, as compared to its leptonic branching ratio to electrons and muons (only 6.7%).

## 5 Conclusion

Very little is known about the nature of the DM and its interaction with the SM particles. It is possible to think of a scenario where DM only couples to the SM leptons, but not to quarks at tree level. We have explored the physics potential of the future  $e^+e^-$  colliders in probing such *leptophilic* DM in a model-independent way. As a case study, we have taken the  $\sqrt{s} = 1$  TeV ILC with an integrated luminosity of  $1000 \text{ fb}^{-1}$  and have analyzed the pair-production of fermionic DM using leptophilic dimension-6 operators of all possible bilinear structures, namely, scalar-pseudoscalar, vector-axialvector and tensor-axialtensor. We have performed a detailed cut-based analysis for each of these operators in three different channels based on the tagged particle, namely, mono-photon, mono- $Z$  leptonic and hadronic.

We have taken into account one of the most important and powerful features of lepton colliders, i.e., the possibility of beam-polarization with different degrees of polarization and helicity orientations. We find that the  $\text{sign}(P(e^-), P(e^+)) = (+, +)$  beam configuration is optimal for the SP and TAT-type operators, while the  $(+, -)$  configuration is better for probing the VA-type operators. The maximum value of the cut-off scale  $\Lambda$  that can be probed in each channel at  $3\sigma$  is given in Table 16. We find that without any systematics, the mono-photon channel provides the best sensitivity across all operator types, while in presence of background systematic effects, the mono- $Z$  hadronic channel provides better sensitivity for the SP and TAT-type operators. A comparison between the sensitivity reaches of different operators can also be seen from Figures 6, 11 and 16.

We also demonstrate the complementarity of our lepton collider study with other existing direct and indirect detection searches for leptophilic DM (cf. Figures 5, 10 and 15). In particular, we show that lepton colliders will be able to provide the best-ever sensitivity in the still unexplored light DM regime.

## Acknowledgments

SK would like to thank Kajari Mazumdar for useful discussions. He would also like to thank Tanumoy Mandal and Suman Kumar Kundu for the help with using ROOT software package. PKD thanks K. C. Kong and Partha Konar for the discussions. BD would like to thank Juri Smirnov for a discussion on the FIMP DM possibility. AG would like thank the Department of Physics, IISER Pune for their support. The work of PKD is partly supported by the SERB Grant No. EMR/2016/002651. The work of BD is supported in part by the US Department of Energy under Grant No. DE-SC0017987 and by a Fermilab Intensity Frontier Fellowship. This work was partly performed at the Aspen Center for Physics, which is supported by National Science Foundation grant PHY-1607611.

## A Kinematic distributions for polarized beams

For completeness, we present in Figures 17, 18 and 19 the kinematic distributions with polarized beams for the same set of variables as shown in Figures 4, 9 and 14 for the mono-photon, mono- $Z$  leptonic and hadronic channels, respectively.

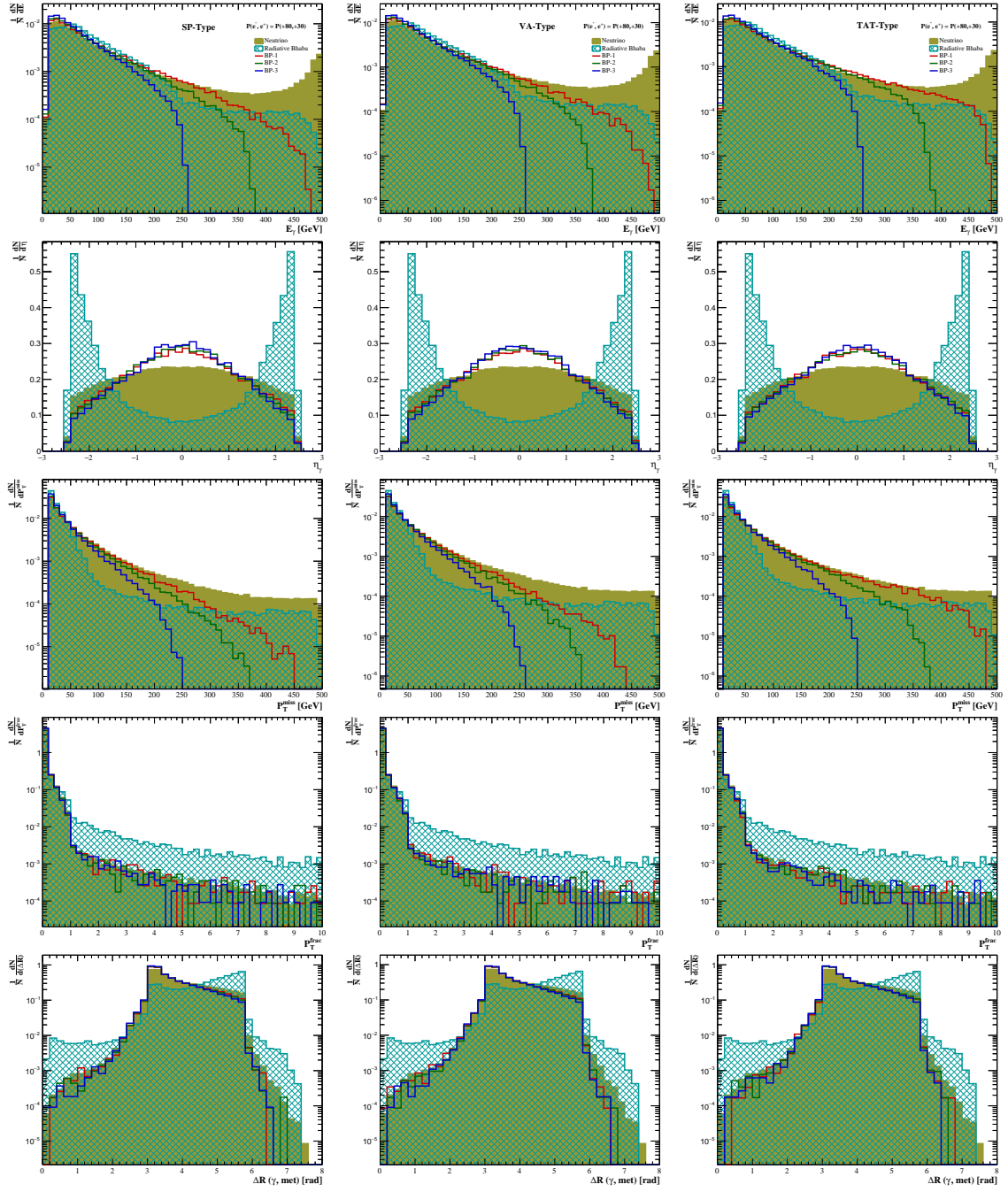


Figure 17: Same as in Figure 4, but for polarized beams with  $P(e^-, e^+) = (+80\%, +30\%)$ .



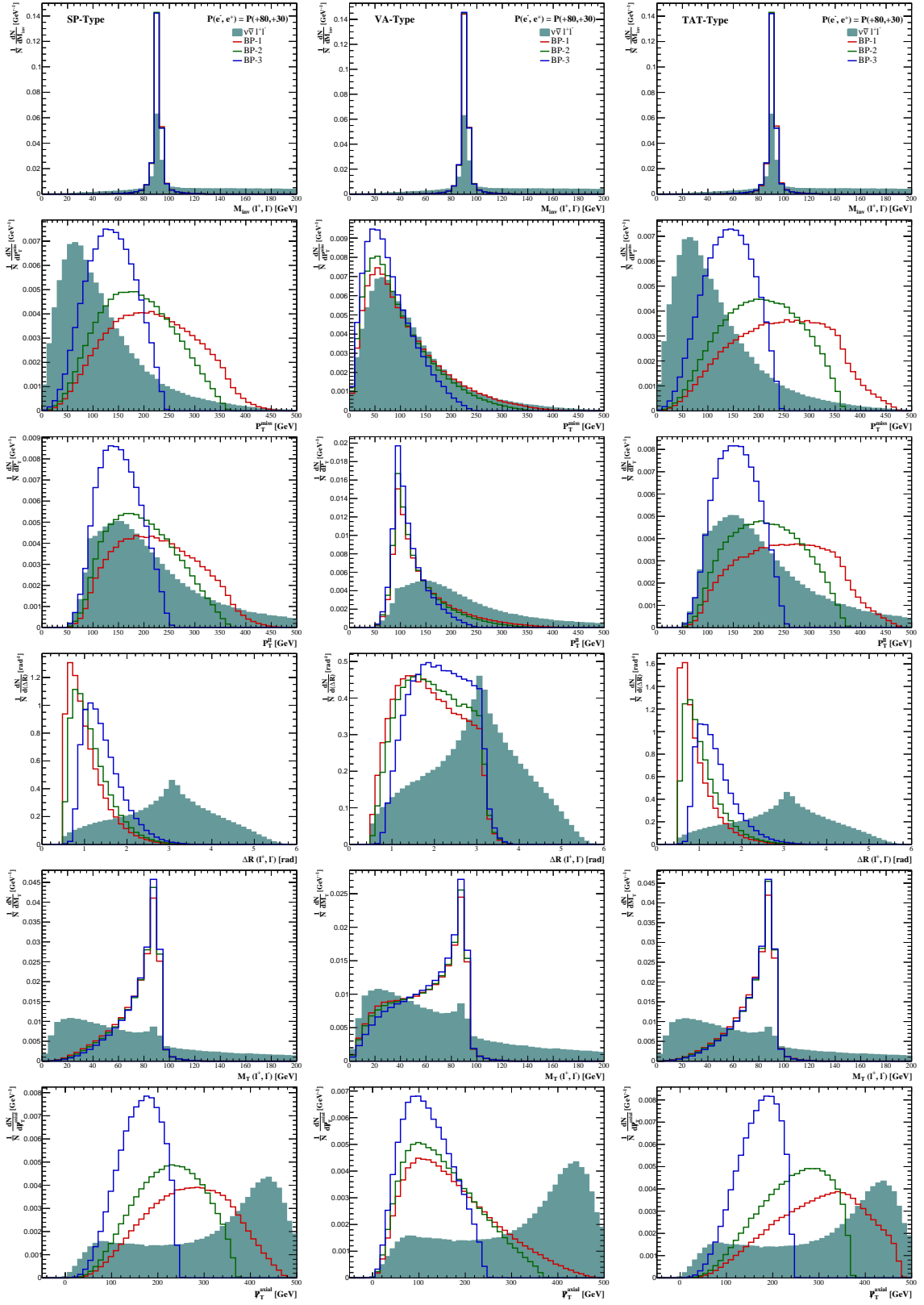
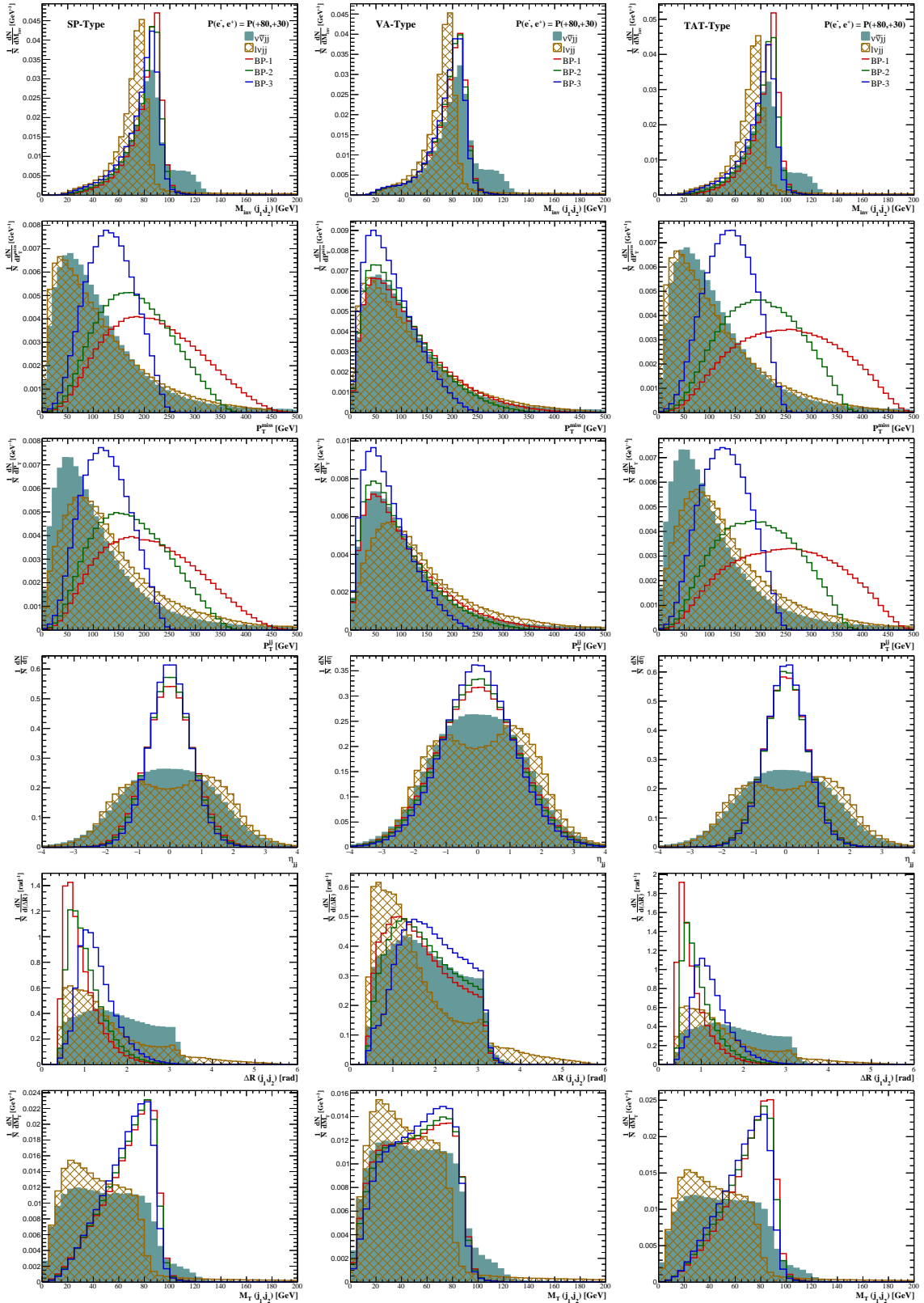


Figure 18: Same as in Figure 9, but with (+80%, +30%) polarized beams.



(continued to next page)

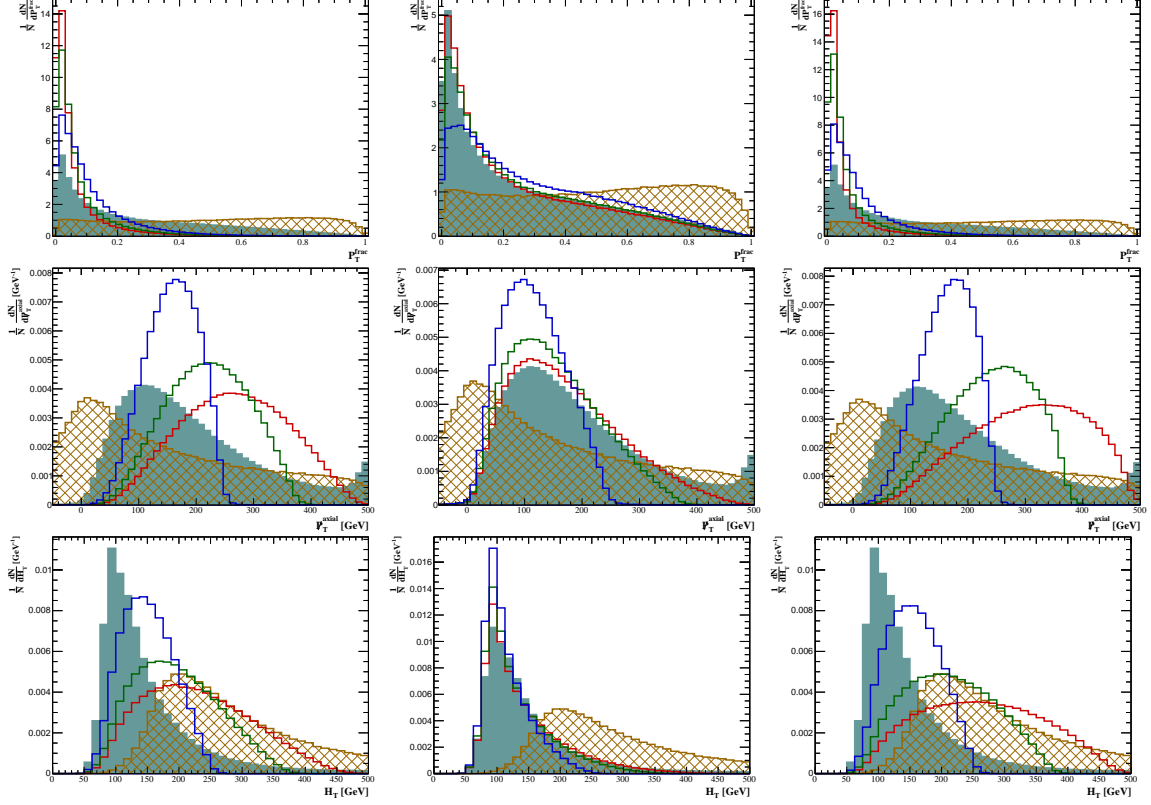


Figure 19: Same as in Figure 14, but with (+80%, +30%) polarized beams.

## References

- [1] G. Bertone, D. Hooper and J. Silk, *Particle dark matter: Evidence, candidates and constraints*, *Phys. Rept.* **405** (2005) 279 [[hep-ph/0404175](#)].
- [2] A.M. Green, *Dark Matter in Astrophysics/Cosmology*, in *Les Houches summer school on Dark Matter*, 9, 2021 [[2109.05854](#)].
- [3] PLANCK collaboration, *Planck 2018 results. VI. Cosmological parameters*, *Astron. Astrophys.* **641** (2020) A6 [[1807.06209](#)].
- [4] G. Bertone and T. Tait, M. P., *A new era in the search for dark matter*, *Nature* **562** (2018) 51 [[1810.01668](#)].
- [5] J. Billard et al., *Direct Detection of Dark Matter – APPEC Committee Report*, [2104.07634](#).
- [6] J.M. Gaskins, *A review of indirect searches for particle dark matter*, *Contemp. Phys.* **57** (2016) 496 [[1604.00014](#)].
- [7] A. Boveia and C. Doglioni, *Dark Matter Searches at Colliders*, *Ann. Rev. Nucl. Part. Sci.* **68** (2018) 429 [[1810.12238](#)].
- [8] M. Battaglieri et al., *US Cosmic Visions: New Ideas in Dark Matter 2017: Community Report*, in *U.S. Cosmic Visions: New Ideas in Dark Matter*, 7, 2017 [[1707.04591](#)].
- [9] J.L. Feng, *Dark Matter Candidates from Particle Physics and Methods of Detection*, *Ann. Rev. Astron. Astrophys.* **48** (2010) 495 [[1003.0904](#)].

- [10] LUX collaboration, *Results from a search for dark matter in the complete LUX exposure*, *Phys. Rev. Lett.* **118** (2017) 021303 [[1608.07648](#)].
- [11] XENON collaboration, *Dark Matter Search Results from a One Ton-Year Exposure of XENON1T*, *Phys. Rev. Lett.* **121** (2018) 111302 [[1805.12562](#)].
- [12] PANDAX-4T collaboration, *Dark Matter Search Results from the PandaX-4T Commissioning Run*, [2107.13438](#).
- [13] J. Billard, L. Strigari and E. Figueroa-Feliciano, *Implication of neutrino backgrounds on the reach of next generation dark matter direct detection experiments*, *Phys. Rev. D* **89** (2014) 023524 [[1307.5458](#)].
- [14] C.A.J. O'Hare, *Fog on the horizon: a new definition of the neutrino floor for direct dark matter searches*, [2109.03116](#).
- [15] L.M. Krauss, S. Nasri and M. Trodden, *A Model for neutrino masses and dark matter*, *Phys. Rev. D* **67** (2003) 085002 [[hep-ph/0210389](#)].
- [16] E.A. Baltz and L. Bergstrom, *Detection of leptonic dark matter*, *Phys. Rev. D* **67** (2003) 043516 [[hep-ph/0211325](#)].
- [17] E. Ma, *Verifiable radiative seesaw mechanism of neutrino mass and dark matter*, *Phys. Rev. D* **73** (2006) 077301 [[hep-ph/0601225](#)].
- [18] T. Hambye, K. Kannike, E. Ma and M. Raidal, *Emanations of Dark Matter: Muon Anomalous Magnetic Moment, Radiative Neutrino Mass, and Novel Leptogenesis at the TeV Scale*, *Phys. Rev. D* **75** (2007) 095003 [[hep-ph/0609228](#)].
- [19] R. Bernabei et al., *Investigating electron interacting dark matter*, *Phys. Rev. D* **77** (2008) 023506 [[0712.0562](#)].
- [20] M. Cirelli, M. Kadastik, M. Raidal and A. Strumia, *Model-independent implications of the  $e^\pm$ , anti-proton cosmic ray spectra on properties of Dark Matter*, *Nucl. Phys. B* **813** (2009) 1 [[0809.2409](#)].
- [21] C.-R. Chen and F. Takahashi, *Cosmic rays from Leptonic Dark Matter*, *JCAP* **02** (2009) 004 [[0810.4110](#)].
- [22] X.-J. Bi, P.-H. Gu, T. Li and X. Zhang, *ATIC and PAMELA Results on Cosmic  $e^\pm$  Excesses and Neutrino Masses*, *JHEP* **04** (2009) 103 [[0901.0176](#)].
- [23] Q.-H. Cao, E. Ma and G. Shaughnessy, *Dark Matter: The Leptonic Connection*, *Phys. Lett. B* **673** (2009) 152 [[0901.1334](#)].
- [24] H.-S. Goh, L.J. Hall and P. Kumar, *The Leptonic Higgs as a Messenger of Dark Matter*, *JHEP* **05** (2009) 097 [[0902.0814](#)].
- [25] X.-J. Bi, X.-G. He and Q. Yuan, *Parameters in a class of leptophilic models from PAMELA, ATIC and FERMI*, *Phys. Lett. B* **678** (2009) 168 [[0903.0122](#)].
- [26] A. Ibarra, A. Ringwald, D. Tran and C. Weniger, *Cosmic Rays from Leptophilic Dark Matter Decay via Kinetic Mixing*, *JCAP* **08** (2009) 017 [[0903.3625](#)].
- [27] H. Davoudiasl, *Dark Matter with Time-Varying Leptophilic Couplings*, *Phys. Rev. D* **80** (2009) 043502 [[0904.3103](#)].
- [28] A. Dedes, I. Giomataris, K. Suxho and J.D. Vergados, *Searching for Secluded Dark Matter via Direct Detection of Recoiling Nuclei as well as Low Energy Electrons*, *Nucl. Phys. B* **826** (2010) 148 [[0907.0758](#)].

- [29] J. Kopp, V. Niro, T. Schwetz and J. Zupan, *DAMA/LIBRA and leptonically interacting Dark Matter*, *Phys. Rev. D* **80** (2009) 083502 [0907.3159].
- [30] T. Cohen and K.M. Zurek, *Leptophilic Dark Matter from the Lepton Asymmetry*, *Phys. Rev. Lett.* **104** (2010) 101301 [0909.2035].
- [31] E.J. Chun, J.-C. Park and S. Scopel, *Dirac gaugino as leptophilic dark matter*, *JCAP* **02** (2010) 015 [0911.5273].
- [32] W. Chao, *Pure Leptonic Gauge Symmetry, Neutrino Masses and Dark Matter*, *Phys. Lett. B* **695** (2011) 157 [1005.1024].
- [33] N. Haba, Y. Kajiyama, S. Matsumoto, H. Okada and K. Yoshioka, *Universally Leptophilic Dark Matter From Non-Abelian Discrete Symmetry*, *Phys. Lett. B* **695** (2011) 476 [1008.4777].
- [34] P. Ko and Y. Omura, *Supersymmetric  $U(1)_B \times U(1)_L$  model with leptophilic and leptophobic cold dark matters*, *Phys. Lett. B* **701** (2011) 363 [1012.4679].
- [35] C.D. Carone and R. Primulando, *A Froggatt-Nielsen Model for Leptophilic Scalar Dark Matter Decay*, *Phys. Rev. D* **84** (2011) 035002 [1105.4635].
- [36] D. Schmidt, T. Schwetz and T. Toma, *Direct Detection of Leptophilic Dark Matter in a Model with Radiative Neutrino Masses*, *Phys. Rev. D* **85** (2012) 073009 [1201.0906].
- [37] M. Das and S. Mohanty, *Leptophilic dark matter in gauged  $L_\mu - L_\tau$  extension of MSSM*, *Phys. Rev. D* **89** (2014) 025004 [1306.4505].
- [38] P.S.B. Dev, D.K. Ghosh, N. Okada and I. Saha, *Neutrino Mass and Dark Matter in light of recent AMS-02 results*, *Phys. Rev. D* **89** (2014) 095001 [1307.6204].
- [39] S. Chang, R. Edezhath, J. Hutchinson and M. Luty, *Leptophilic Effective WIMPs*, *Phys. Rev. D* **90** (2014) 015011 [1402.7358].
- [40] P. Agrawal, Z. Chacko and C.B. Verhaaren, *Leptophilic Dark Matter and the Anomalous Magnetic Moment of the Muon*, *JHEP* **08** (2014) 147 [1402.7369].
- [41] N.F. Bell, Y. Cai, R.K. Leane and A.D. Medina, *Leptophilic dark matter with  $Z'$  interactions*, *Phys. Rev. D* **90** (2014) 035027 [1407.3001].
- [42] A. Freitas and S. Westhoff, *Leptophilic Dark Matter in Lepton Interactions at LEP and ILC*, *JHEP* **10** (2014) 116 [1408.1959].
- [43] Q.-H. Cao, C.-R. Chen and T. Gong, *Leptophilic dark matter confronts AMS-02 cosmic-ray positron flux*, *Chin. J. Phys.* **55** (2017) 10 [1409.7317].
- [44] S.M. Boucenna, M. Chianese, G. Mangano, G. Miele, S. Morisi, O. Pisanti et al., *Decaying Leptophilic Dark Matter at IceCube*, *JCAP* **12** (2015) 055 [1507.01000].
- [45] B.-Q. Lu and H.-S. Zong, *Leptophilic dark matter in Galactic Center excess*, *Phys. Rev. D* **93** (2016) 083504.
- [46] G.H. Duan, L. Feng, F. Wang, L. Wu, J.M. Yang and R. Zheng, *Simplified TeV leptophilic dark matter in light of DAMPE data*, *JHEP* **02** (2018) 107 [1711.11012].
- [47] G.H. Duan, X.-G. He, L. Wu and J.M. Yang, *Leptophilic dark matter in gauged  $U(1)_{L_e - L_\mu}$  model in light of DAMPE cosmic ray  $e^+ + e^-$  excess*, *Eur. Phys. J. C* **78** (2018) 323 [1711.11563].

- [48] W. Chao, H.-K. Guo, H.-L. Li and J. Shu, *Electron Flavored Dark Matter*, *Phys. Lett. B* **782** (2018) 517 [[1712.00037](#)].
- [49] T. Li, N. Okada and Q. Shafi, *Scalar dark matter, Type II Seesaw and the DAMPE cosmic ray  $e^+ + e^-$  excess*, *Phys. Lett. B* **779** (2018) 130 [[1712.00869](#)].
- [50] K. Ghorbani and P.H. Ghorbani, *DAMPE electron-positron excess in leptophilic  $Z'$  model*, *JHEP* **05** (2018) 125 [[1712.01239](#)].
- [51] Y. Sui and Y. Zhang, *Prospects of type-II seesaw models at future colliders in light of the DAMPE  $e^+e^-$  excess*, *Phys. Rev. D* **97** (2018) 095002 [[1712.03642](#)].
- [52] Z.-L. Han, W. Wang and R. Ding, *Radiative Seesaw Model and DAMPE Excess from Leptophilic Gauge Symmetry*, *Eur. Phys. J. C* **78** (2018) 216 [[1712.05722](#)].
- [53] E. Madge and P. Schwaller, *Leptophilic dark matter from gauged lepton number: Phenomenology and gravitational wave signatures*, *JHEP* **02** (2019) 048 [[1809.09110](#)].
- [54] S. Junius, L. Lopez-Honorez and A. Mariotti, *A feeble window on leptophilic dark matter*, *JHEP* **07** (2019) 136 [[1904.07513](#)].
- [55] S. Yaser Ayazi and A. Mohamadnejad, *DAMPE excess from leptophilic vector dark matter: a model-independent approach*, *J. Phys. G* **47** (2020) 095003 [[1909.10729](#)].
- [56] S. Ghosh, A. Dutta Banik, E.J. Chun and D. Majumdar, *Leptophilic-portal Dark Matter in the Light of AMS-02 positron excess*, [2003.07675](#).
- [57] S. Chakraborti and R. Islam, *Implications of dark sector mixing on leptophilic scalar dark matter*, *JHEP* **03** (2021) 032 [[2007.13719](#)].
- [58] S.-I. Horigome, T. Katayose, S. Matsumoto and I. Saha, *Leptophilic fermion WIMP: Role of future lepton colliders*, *Phys. Rev. D* **104** (2021) 055001 [[2102.08645](#)].
- [59] R. Garani, F. Gasparotto, P. Mastrolia, H.J. Munch, S. Palomares-Ruiz and A. Primo, *Two-photon exchange in leptophilic dark matter scenarios*, [2105.12116](#).
- [60] MUON G-2 collaboration, *Final Report of the Muon E821 Anomalous Magnetic Moment Measurement at BNL*, *Phys. Rev. D* **73** (2006) 072003 [[hep-ex/0602035](#)].
- [61] MUON G-2 collaboration, *Measurement of the Positive Muon Anomalous Magnetic Moment to 0.46 ppm*, *Phys. Rev. Lett.* **126** (2021) 141801 [[2104.03281](#)].
- [62] DAMA/LIBRA collaboration, *The DAMA project: Achievements, implications and perspectives*, *Prog. Part. Nucl. Phys.* **114** (2020) 103810.
- [63] ATIC collaboration, *An excess of cosmic ray electrons at energies of 300-800 GeV*, *Nature* **456** (2008) 362.
- [64] PAMELA collaboration, *An anomalous positron abundance in cosmic rays with energies 1.5-100 GeV*, *Nature* **458** (2009) 607 [[0810.4995](#)].
- [65] PAMELA collaboration, *Cosmic-Ray Positron Energy Spectrum Measured by PAMELA*, *Phys. Rev. Lett.* **111** (2013) 081102 [[1308.0133](#)].
- [66] FERMI-LAT collaboration, *Measurement of separate cosmic-ray electron and positron spectra with the Fermi Large Area Telescope*, *Phys. Rev. Lett.* **108** (2012) 011103 [[1109.0521](#)].
- [67] FERMI-LAT collaboration, *Cosmic-ray electron-positron spectrum from 7 GeV to 2 TeV with the Fermi Large Area Telescope*, *Phys. Rev. D* **95** (2017) 082007 [[1704.07195](#)].

- [68] AMS collaboration, *High Statistics Measurement of the Positron Fraction in Primary Cosmic Rays of 0.5–500 GeV with the Alpha Magnetic Spectrometer on the International Space Station*, *Phys. Rev. Lett.* **113** (2014) 121101.
- [69] AMS collaboration, *Electron and Positron Fluxes in Primary Cosmic Rays Measured with the Alpha Magnetic Spectrometer on the International Space Station*, *Phys. Rev. Lett.* **113** (2014) 121102.
- [70] AMS collaboration, *The Alpha Magnetic Spectrometer (AMS) on the international space station: Part II — Results from the first seven years*, *Phys. Rept.* **894** (2021) 1.
- [71] DAMPE collaboration, *Direct detection of a break in the teraelectronvolt cosmic-ray spectrum of electrons and positrons*, *Nature* **552** (2017) 63 [1711.10981].
- [72] CALET collaboration, *Extended Measurement of the Cosmic-Ray Electron and Positron Spectrum from 11 GeV to 4.8 TeV with the Calorimetric Electron Telescope on the International Space Station*, *Phys. Rev. Lett.* **120** (2018) 261102 [1806.09728].
- [73] FERMI-LAT collaboration, *Fermi-LAT Observations of High-Energy  $\gamma$ -Ray Emission Toward the Galactic Center*, *Astrophys. J.* **819** (2016) 44 [1511.02938].
- [74] T. Siebert, R. Diehl, G. Khachatryan, M.G.H. Krause, F. Guglielmetti, J. Greiner et al., *Gamma-ray spectroscopy of Positron Annihilation in the Milky Way*, *Astron. Astrophys.* **586** (2016) A84 [1512.00325].
- [75] ICECUBE collaboration, *The IceCube high-energy starting event sample: Description and flux characterization with 7.5 years of data*, 2011.03545.
- [76] XENON collaboration, *Excess electronic recoil events in XENON1T*, *Phys. Rev. D* **102** (2020) 072004 [2006.09721].
- [77] XENON100 collaboration, *Exclusion of Leptophilic Dark Matter Models using XENON100 Electronic Recoil Data*, *Science* **349** (2015) 851 [1507.07747].
- [78] XENON collaboration, *Light Dark Matter Search with Ionization Signals in XENON1T*, *Phys. Rev. Lett.* **123** (2019) 251801 [1907.11485].
- [79] LZ collaboration, *Projected sensitivities of the LUX-ZEPLIN (LZ) experiment to new physics via low-energy electron recoils*, 2102.11740.
- [80] C.-Y. Chen, J. Kozaczuk and Y.-M. Zhong, *Exploring leptophilic dark matter with NA64- $\mu$* , *JHEP* **10** (2018) 154 [1807.03790].
- [81] L. Marsicano, M. Battaglieri, A. Celentano, R. De Vita and Y.-M. Zhong, *Probing Leptophilic Dark Sectors at Electron Beam-Dump Facilities*, *Phys. Rev. D* **98** (2018) 115022 [1812.03829].
- [82] B. Chauhan and S. Mohanty, *Constraints on leptophilic light dark matter from internal heat flux of Earth*, *Phys. Rev. D* **94** (2016) 035024 [1603.06350].
- [83] R. Garani and S. Palomares-Ruiz, *Dark matter in the Sun: scattering off electrons vs nucleons*, *JCAP* **05** (2017) 007 [1702.02768].
- [84] Z.-L. Liang, Y.-L. Tang and Z.-Q. Yang, *The leptophilic dark matter in the Sun: the minimum testable mass*, *JCAP* **10** (2018) 035 [1802.01005].
- [85] A. Guha, P.S.B. Dev and P.K. Das, *Model-independent Astrophysical Constraints on Leptophilic Dark Matter in the Framework of Tsallis Statistics*, *JCAP* **02** (2019) 032 [1810.00399].

- [86] N.F. Bell, G. Busoni and S. Robles, *Capture of Leptophilic Dark Matter in Neutron Stars*, *JCAP* **06** (2019) 054 [[1904.09803](#)].
- [87] R. Garani and J. Heeck, *Dark matter interactions with muons in neutron stars*, *Phys. Rev. D* **100** (2019) 035039 [[1906.10145](#)].
- [88] A. Joglekar, N. Raj, P. Tanedo and H.-B. Yu, *Relativistic capture of dark matter by electrons in neutron stars*, *Phys. Lett. B* (2020) 135767 [[1911.13293](#)].
- [89] A. Joglekar, N. Raj, P. Tanedo and H.-B. Yu, *Dark kinetic heating of neutron stars from contact interactions with relativistic targets*, *Phys. Rev. D* **102** (2020) 123002 [[2004.09539](#)].
- [90] N.F. Bell, G. Busoni, S. Robles and M. Virgato, *Improved Treatment of Dark Matter Capture in Neutron Stars II: Leptonic Targets*, *JCAP* **03** (2021) 086 [[2010.13257](#)].
- [91] M. Beltran, D. Hooper, E.W. Kolb, Z.A.C. Krusberg and T.M.P. Tait, *Maverick dark matter at colliders*, *JHEP* **09** (2010) 037 [[1002.4137](#)].
- [92] J. Goodman, M. Ibe, A. Rajaraman, W. Shepherd, T.M.P. Tait and H.-B. Yu, *Constraints on Light Majorana dark Matter from Colliders*, *Phys. Lett. B* **695** (2011) 185 [[1005.1286](#)].
- [93] Y. Bai, P.J. Fox and R. Harnik, *The Tevatron at the Frontier of Dark Matter Direct Detection*, *JHEP* **12** (2010) 048 [[1005.3797](#)].
- [94] J. Goodman, M. Ibe, A. Rajaraman, W. Shepherd, T.M.P. Tait and H.-B. Yu, *Constraints on Dark Matter from Colliders*, *Phys. Rev. D* **82** (2010) 116010 [[1008.1783](#)].
- [95] P.J. Fox, R. Harnik, J. Kopp and Y. Tsai, *LEP Shines Light on Dark Matter*, *Phys. Rev. D* **84** (2011) 014028 [[1103.0240](#)].
- [96] P.J. Fox, R. Harnik, J. Kopp and Y. Tsai, *Missing Energy Signatures of Dark Matter at the LHC*, *Phys. Rev. D* **85** (2012) 056011 [[1109.4398](#)].
- [97] A. Rajaraman, W. Shepherd, T.M.P. Tait and A.M. Wijangco, *LHC Bounds on Interactions of Dark Matter*, *Phys. Rev. D* **84** (2011) 095013 [[1108.1196](#)].
- [98] Y.J. Chae and M. Perelstein, *Dark Matter Search at a Linear Collider: Effective Operator Approach*, *JHEP* **05** (2013) 138 [[1211.4008](#)].
- [99] F. Kahlhoefer, *Review of LHC Dark Matter Searches*, *Int. J. Mod. Phys. A* **32** (2017) 1730006 [[1702.02430](#)].
- [100] B. Penning, *The pursuit of dark matter at colliders—an overview*, *J. Phys. G* **45** (2018) 063001 [[1712.01391](#)].
- [101] CMS collaboration, *Search for dark matter, extra dimensions, and unparticles in monojet events in proton–proton collisions at  $\sqrt{s} = 8$  TeV*, *Eur. Phys. J. C* **75** (2015) 235 [[1408.3583](#)].
- [102] ATLAS collaboration, *Search for new phenomena in final states with an energetic jet and large missing transverse momentum in pp collisions at  $\sqrt{s} = 8$  TeV with the ATLAS detector*, *Eur. Phys. J. C* **75** (2015) 299 [[1502.01518](#)].
- [103] CMS collaboration, *Search for new physics in final states with an energetic jet or a hadronically decaying W or Z boson and transverse momentum imbalance at  $\sqrt{s} = 13$  TeV*, *Phys. Rev. D* **97** (2018) 092005 [[1712.02345](#)].
- [104] ATLAS collaboration, *Search for new phenomena in events with an energetic jet and missing transverse momentum in pp collisions at  $\sqrt{s} = 13$  TeV with the ATLAS detector*, *Phys. Rev. D* **103** (2021) 112006 [[2102.10874](#)].



- [105] L.A. Cavasonza, H. Gast, M. Krämer, M. Pellen and S. Schael, *Constraints on leptophilic dark matter from the AMS-02 experiment*, *Astrophys. J.* **839** (2017) 36 [[1612.06634](#)].
- [106] I. John and T. Linden, *Cosmic-Ray Positrons Strongly Constrain Leptophilic Dark Matter*, [2107.10261](#).
- [107] DELPHI collaboration, *Photon events with missing energy in  $e^+e^-$  collisions at  $s^{**}(1/2) = 130\text{-GeV}$  to  $209\text{-GeV}$* , *Eur. Phys. J. C* **38** (2005) 395 [[hep-ex/0406019](#)].
- [108] A. Birkedal, K. Matchev and M. Perelstein, *Dark matter at colliders: A Model independent approach*, *Phys. Rev. D* **70** (2004) 077701 [[hep-ph/0403004](#)].
- [109] P.J. Fox and E. Poppitz, *Leptophilic Dark Matter*, *Phys. Rev. D* **79** (2009) 083528 [[0811.0399](#)].
- [110] P. Konar, K. Kong, K.T. Matchev and M. Perelstein, *Shedding Light on the Dark Sector with Direct WIMP Production*, *New J. Phys.* **11** (2009) 105004 [[0902.2000](#)].
- [111] C. Bartels, M. Berggren and J. List, *Characterising WIMPs at a future  $e^+e^-$  Linear Collider*, *Eur. Phys. J. C* **72** (2012) 2213 [[1206.6639](#)].
- [112] H. Dreiner, M. Huck, M. Krämer, D. Schmeier and J. Tattersall, *Illuminating Dark Matter at the ILC*, *Phys. Rev. D* **87** (2013) 075015 [[1211.2254](#)].
- [113] Z. Liu, Y.-H. Xu and Y. Zhang, *Probing dark matter particles at CEPC*, *JHEP* **06** (2019) 009 [[1903.12114](#)].
- [114] M. Habermehl, M. Berggren and J. List, *WIMP Dark Matter at the International Linear Collider*, *Phys. Rev. D* **101** (2020) 075053 [[2001.03011](#)].
- [115] J. Kalinowski, W. Kotlarski, K. Mekala, P. Sopicki and A.F. Zarnecki, *Sensitivity of future  $e^+e^-$  colliders to processes of dark matter production with light mediator exchange*, [2107.11194](#).
- [116] B. Barman, S. Bhattacharya, S. Girmohanta and S. Jahedi, *Catch 'em all: Effective Leptophilic WIMPs at the  $e^+e^-$  Collider*, [2109.10936](#).
- [117] N. Wan, M. Song, G. Li, W.-G. Ma, R.-Y. Zhang and J.-Y. Guo, *Searching for dark matter via mono- $Z$  boson production at the ILC*, *Eur. Phys. J. C* **74** (2014) 3219 [[1403.7921](#)].
- [118] Z.-H. Yu, X.-J. Bi, Q.-S. Yan and P.-F. Yin, *Dark matter searches in the mono- $Z$  channel at high energy  $e^+e^-$  colliders*, *Phys. Rev. D* **90** (2014) 055010 [[1404.6990](#)].
- [119] S. Dutta, D. Sachdeva and B. Rawat, *Signals of Leptophilic Dark Matter at the ILC*, *Eur. Phys. J. C* **77** (2017) 639 [[1704.03994](#)].
- [120] B. Grzadkowski, M. Igllicki, K. Mekala and A.F. Zarnecki, *Dark-matter-spin effects at future  $e^+e^-$  colliders*, *JHEP* **08** (2020) 052 [[2003.06719](#)].
- [121] P. Bambade et al., *The International Linear Collider: A Global Project*, [1903.01629](#).
- [122] CLIC, CLICDP collaboration, *Updated baseline for a staged Compact Linear Collider*, [1608.07537](#).
- [123] CEPC STUDY GROUP collaboration, *CEPC Conceptual Design Report: Volume 2 - Physics & Detector*, [1811.10545](#).
- [124] FCC collaboration, *FCC-ee: The Lepton Collider: Future Circular Collider Conceptual Design Report Volume 2*, *Eur. Phys. J. ST* **228** (2019) 261.

- [125] T. Barklow, J. Brau, K. Fujii, J. Gao, J. List, N. Walker et al., *ILC Operating Scenarios*, [1506.07830](#).
- [126] J.P. Delahaye, M. Diemoz, K. Long, B. Mansoulié, N. Pastrone, L. Rivkin et al., *Muon Colliders*, [1901.06150](#).
- [127] S. Matsumoto, S. Mukhopadhyay and Y.-L.S. Tsai, *Effective Theory of WIMP Dark Matter supplemented by Simplified Models: Singlet-like Majorana fermion case*, *Phys. Rev. D* **94** (2016) 065034 [[1604.02230](#)].
- [128] G. Busoni, A. De Simone, E. Morgante and A. Riotto, *On the Validity of the Effective Field Theory for Dark Matter Searches at the LHC*, *Phys. Lett. B* **728** (2014) 412 [[1307.2253](#)].
- [129] J. Alwall, P. Schuster and N. Toro, *Simplified Models for a First Characterization of New Physics at the LHC*, *Phys. Rev. D* **79** (2009) 075020 [[0810.3921](#)].
- [130] J. Abdallah et al., *Simplified Models for Dark Matter Searches at the LHC*, *Phys. Dark Univ.* **9-10** (2015) 8 [[1506.03116](#)].
- [131] A. Belyaev, N.D. Christensen and A. Pukhov, *CalcHEP 3.4 for collider physics within and beyond the Standard Model*, *Comput. Phys. Commun.* **184** (2013) 1729 [[1207.6082](#)].
- [132] A. Alloul, N.D. Christensen, C. Degrande, C. Duhr and B. Fuks, *FeynRules 2.0 - A complete toolbox for tree-level phenomenology*, *Comput. Phys. Commun.* **185** (2014) 2250 [[1310.1921](#)].
- [133] W. Kilian, T. Ohl and J. Reuter, *WHIZARD: Simulating Multi-Particle Processes at LHC and ILC*, *Eur. Phys. J. C* **71** (2011) 1742 [[0708.4233](#)].
- [134] H. Abramowicz et al., *The International Linear Collider Technical Design Report - Volume 4: Detectors*, [1306.6329](#).
- [135] DELPHES 3 collaboration, *DELPHES 3, A modular framework for fast simulation of a generic collider experiment*, *JHEP* **02** (2014) 057 [[1307.6346](#)].
- [136] C.T. Potter, *DSiD: a Delphes Detector for ILC Physics Studies*, in *International Workshop on Future Linear Colliders*, 2, 2016 [[1602.07748](#)].
- [137] H. Abramowicz et al., *Forward Instrumentation for ILC Detectors*, *JINST* **5** (2010) P12002 [[1009.2433](#)].
- [138] A. Hocker et al., *TMVA - Toolkit for Multivariate Data Analysis*, [physics/0703039](#).
- [139] L. Hamaide and C. McCabe, *Fuelling the search for light dark matter-electron scattering*, [2110.02985](#).
- [140] R.K. Leane, T.R. Slatyer, J.F. Beacom and K.C.Y. Ng, *GeV-scale thermal WIMPs: Not even slightly ruled out*, *Phys. Rev. D* **98** (2018) 023016 [[1805.10305](#)].
- [141] G. Steigman, B. Dasgupta and J.F. Beacom, *Precise Relic WIMP Abundance and its Impact on Searches for Dark Matter Annihilation*, *Phys. Rev. D* **86** (2012) 023506 [[1204.3622](#)].
- [142] L.J. Hall, K. Jedamzik, J. March-Russell and S.M. West, *Freeze-In Production of FIMP Dark Matter*, *JHEP* **03** (2010) 080 [[0911.1120](#)].
- [143] J. Alwall, R. Frederix, S. Frixione, V. Hirschi, F. Maltoni, O. Mattelaer et al., *The automated computation of tree-level and next-to-leading order differential cross sections, and their matching to parton shower simulations*, *JHEP* **07** (2014) 079 [[1405.0301](#)].

- [144] S. Frixione, E. Laenen, P. Motylinski and B.R. Webber, *Angular correlations of lepton pairs from vector boson and top quark decays in Monte Carlo simulations*, *JHEP* **04** (2007) 081 [[hep-ph/0702198](#)].
- [145] P. Artoisenet, R. Frederix, O. Mattelaer and R. Rietkerk, *Automatic spin-entangled decays of heavy resonances in Monte Carlo simulations*, *JHEP* **03** (2013) 015 [[1212.3460](#)].
- [146] N.F. Bell, J.B. Dent, A.J. Galea, T.D. Jacques, L.M. Krauss and T.J. Weiler, *Searching for Dark Matter at the LHC with a Mono-Z*, *Phys. Rev. D* **86** (2012) 096011 [[1209.0231](#)].
- [147] ATLAS collaboration, *Measurement of ZZ production in pp collisions at  $\sqrt{s} = 7$  TeV and limits on anomalous ZZZ and ZZ $\gamma$  couplings with the ATLAS detector*, *JHEP* **03** (2013) 128 [[1211.6096](#)].
- [148] L.M. Carpenter, A. Nelson, C. Shimmin, T.M.P. Tait and D. Whiteson, *Collider searches for dark matter in events with a Z boson and missing energy*, *Phys. Rev. D* **87** (2013) 074005 [[1212.3352](#)].
- [149] A. Alves and K. Sinha, *Searches for Dark Matter at the LHC: A Multivariate Analysis in the Mono-Z Channel*, *Phys. Rev. D* **92** (2015) 115013 [[1507.08294](#)].
- [150] A. Adhikary, B. Bhattacharjee, R.M. Godbole, N. Khan and S. Kulkarni, *Searching for heavy Higgs in supersymmetric final states at the LHC*, *JHEP* **04** (2021) 284 [[2002.07137](#)].
- [151] A.J. Barr, *Measuring slepton spin at the LHC*, *JHEP* **02** (2006) 042 [[hep-ph/0511115](#)].
- [152] T. Sjöstrand, S. Ask, J.R. Christiansen, R. Corke, N. Desai, P. Ilten et al., *An introduction to PYTHIA 8.2*, *Comput. Phys. Commun.* **191** (2015) 159 [[1410.3012](#)].
- [153] M. Cacciari, G.P. Salam and G. Soyez, *The anti- $k_t$  jet clustering algorithm*, *JHEP* **04** (2008) 063 [[0802.1189](#)].
- [154] M. Cacciari, G.P. Salam and G. Soyez, *FastJet User Manual*, *Eur. Phys. J. C* **72** (2012) 1896 [[1111.6097](#)].